Optimal Nonlinear Robust Sliding Mode Control of an Excitation System Based on Mixed $\mathcal{H}_2 / \mathcal{H}_\infty$ Linear Matrix Inequalities

Yidong Zou, Yunhe Wang, Jinbao Chen, Wenqing Hu, Yang Zheng, Wenhao Sun, and Zhihuai Xiao

***Abstract*—In this paper, an optimal nonlinear robust sliding mode control (ONRSMC) based on mixed $\mathcal{H}_2 / \mathcal{H}_\infty$ linear matrix inequalities (LMIs) is designed for the excitation system in a "one machine-infinite bus system" (OMIBS) to enhance system stability. Initially, the direct feedback linearization method is used to establish a mathematical model of the OMIBS incorporating uncertainties. ONRSMC is then designed for this model, employing the mixed $\mathcal{H}_2 / \mathcal{H}_\infty$ LMIs. The chaos mapping-based adaptive salp swarm algorithm (CASSA) is introduced to fully optimize the parameters of the sliding mode control, ensuring optimal performance under a specified condition. CASSA demonstrates rapid convergence and reduced likelihood of falling into local optima during optimization. Finally, ONRSMC is obtained through inverse transformation, exhibiting the advantages of simple structure, high reliability, and independence from the accuracy of system models. Four simulation scenarios are employed to validate the effectiveness and robustness of ONRSMC, including mechanical power variation, generator three-phase short circuit, transmission line short circuit, and generator parameter uncertainty. The results indicate that ONRSMC achieves optimal dynamic performance in various operating conditions, facilitating the stable operation of power systems following faults.**

***Index Terms*—Excitation, sliding mode, linear matrix inequality, salp swarm algorithm.**

I. Introduction

The excitation system of a generator is an essential component of the power system, and excitation control is one of the most economical and effective techniques for enhancing power system stability [1], [2]. Generator excitation systems mainly affect the grid voltage levels and the distribution of reactive power among parallel operating units [3]. In certain fault conditions, a decrease in generator terminal voltage will reduce power system stability [4]. Therefore, when a fault occurs, it is necessary to rapidly increase the generator's excitation current to maintain the grid voltage level and stability [5]. Thus, automatic control of synchronous generator excitation plays a critical role in ensuring power quality, rational distribution of reactive power, and improving the reliability of power system operation [6], [7].

Various methods have been proposed to improve the stability of power systems [8], and many improved control strategies for excitation systems have emerged. Currently, the widely used improved control strategy in excitation systems is the proportional-integral-derivative controller and power system stabilizer (PID+PSS) excitation control method [9]. This method is based on conventional PID control which incorporates auxiliary excitation control to form a dual-input control structure of PID+PSS [10]. Specifically, active power, generator speed, and system frequency deviations are added to the feedback inputs. The advantage of PID+PSS control is that it can compensate for the phase lag caused by the excitation system under single PID control, making the dominant pole of the original system transfer function further away from the imaginary axis, thus increasing system damping, improving system anti-interference ability, and effectively suppressing low-frequency oscillations in the system [11]. Also, PSS has a simple control structure, so it is widely used in practical power systems [12]. However, the PID+PSS control method also has some disadvantages. As the design of PSS is typically carried out in a selected network model and oscillation space, designing under specified operating conditions may exacerbate the harm of oscillation to the system when the actual frequency deviates from the set value. In addition, according to the working principle of PSS, it is an additional univariate excitation control method. Optimized parameter design may still result in the system not achieving the best control effect.

In reality, power systems are multi-objective and strongly nonlinear systems, making it difficult for the classical control theory of PID+PSS to meet the real

Received: August 28, 2023
Accepted: January 23, 2024
Published Online: July 1, 2024
Yidong Zou, Yunhe Wang, Jinbao Chen, Wenqing Hu, Yang Zheng, Wenhao Sun and Zhihuai Xiao (corresponding author) are with the School of Power and Mechanical Engineering, Wuhan University, Wuhan 430072, China (e-mail: yidongzou@whu.edu.cn; 2013301390055@whu.edu.cn; 13253681095@163.com; wenqinghu@whu.edu.cn; zhengyang@whu.edu.cn; sunwenhao@whu.edu.cn; xiaozhihuai@126.com).
DOI: 10.23919/PCMP.2023.000325

needs of power systems [13]. In order to achieve control with certain objective constraints, linear optimal excitation control (LOEC) is proposed in [14]. The method involves forming a control quantity by superimposing multiple output deviations of the generator according to a preset ratio, and the system state equation and quadratic performance index are then linearized at a specific generator operating point to obtain feedback coefficients [15]. This control method can also design control laws specifically for different control objects, offering better dynamic performance than PSS, with improved robustness, damping characteristics, adaptability, and higher static stability limit for the system [16]. However, the design of the LOEC is carried out at a certain operating equilibrium point of the system. Therefore, although the excitation system performs well in steady-state or small disturbances, it will result in static errors if a large disturbance causes the system to deviate from the initial operating point or system topology change.

When a system exhibits low sensitivity to uncertain disturbances in key indicators such as stability, disturbance rejection, and optimal performance, it can be said to possess robustness [17]. Robust control involves the application of specific control methods to enable a system to obtain control strategies with robust properties [18], [19]. In the study of control strategies for excitation systems, there has been extensive research on the application of robust control [20]. In [21], a robust sliding mode controller (RSMC) based on a disturbance observer is proposed for the control of excitation systems. It also improves the stability of the power system. In [22], an optimized robust excitation system controller is designed to cope with the uncertainty of power system model parameters, whereas [23] develops a synchronous generator excitation controller, based on an innovative feed forward control strategy, to enhance the system's dynamic response speed and robust performance. Robust excitation control design methods also include $\mathcal{H}_\infty$ [24], [25], $\mathcal{H}_2$ [26], linear quadratic optimal regulator (LQR) gain [27], μ-analysis [28], [29], and mixed $\mathcal{H}_2 / \mathcal{H}_\infty$ controls [30]–[32]. The control strategy designed by the $\mathcal{H}_\infty$ method can effectively reduce the impact of disturbance on system output and handle uncertain system models. The combined method simplifies the calculation process of time-domain simulation to ensure computational accuracy, thus reducing the conservatism of the general $\mathcal{H}_\infty$ analysis method. $\mathcal{H}_2$ control is a disturbance attenuation robust control theory with the core idea of reducing the sensitivity of the output to disturbance signals through control. However, selecting weighting functions in these robust controller designs is highly dependent on the designer's experience.

Artificial intelligence technology is rapidly advancing [33] resulting from combining artificial intelligence and control theory [34]. Intelligent control can process nonlinear, adaptive, and self-learning characteristics without relying on specific system models [35]. As a result, it is particularly well suited for excitation control of power systems with strong nonlinearity and time-varying characteristics. Therefore, a multitude of intelligent control methods, including fuzzy [36]–[38], intelligent optimization algorithm [39]–[42], and neural network control, have been employed for excitation control of generators [43], [44]. However, intelligent control methods have some limitations. For instance, fuzzy control is sensitive to the scale of control rules. If the control rules are too simple, it can significantly reduce the system's control accuracy and produce less than ideal dynamic processes [45]. Conversely, overly complex control rules can increase the search space, reduce decision-making speed, and prevent the system from responding in real-time, potentially hindering the ability to achieve effective control [46]. Neural network control methods lack a clear physical interpretation, and selecting the network structure, number of hidden layers, and neurons per layer lacks comprehensive theoretical support. Conducting stability analysis for neural network control systems is relatively challenging, and convergence cannot always be guaranteed. Additionally, neural network algorithms are prone to getting trapped in local optima, necessitating their combination with other control methods [47]. Despite these limitations, the advance of computer processing power and advanced algorithms has greatly expanded the potentials for further development and application of intelligent excitation control.

Traditional linear excitation control methods are simple and straightforward to implement. However, their inherent limitations hinder them from achieving satisfactory control effects in complex operating conditions and high-efficiency requirements [48]. In contrast, nonlinear excitation control, through in-depth investigation of generator's internal nonlinear characteristics, can better adapt to diverse operating environments and attain higher performance benchmarks [49]. Consequently, nonlinear excitation control holds significant potential for enhancing generator stability and efficient operation. In recent years, the field of nonlinear excitation control has seen considerable advances, including model predictive control-based nonlinear excitation [50], [51], feedback linearization-based nonlinear excitation [52], adaptive backstepping robust nonlinear excitation [53], [54], and fuzzy logic-based nonlinear excitation control techniques [55]. These innovative control methods not only improve generator dynamic performance but also substantially decrease system sensitivity to disturbances, providing robust support for stable operation. Despite the remarkable achievements in both theoretical research and practical application of nonlinear excitation control technology, numerous challenges and problems remain to be addressed, including the complexity of controller design, high computational load, and stringent real-time requirements.

From reviewing the research on excitation control, some problems can be observed. The design of PID control and PSS is based on an approximately linearized model at a certain equilibrium state, and therefore there may not be acceptable damping in some cases. The LQR adopts a typical optimal control method with a linear quadratic performance index. However, optimal control theory relies on a precise mathematical model of the controlled object, without considering the effect of model errors. However, in actual control systems, the existence of model errors is unavoidable, and this limits the application of optimal control theory. LOEC and nonlinear excitation control (NEC) based on modern control theory use fixed structures and parameters in their modeling, without considering the uncertainty of the model, so the designed controllers also struggle to achieve the expected performance.

In order to overcome the shortcomings of the existing excitation controllers, this paper considers the influence of uncertainty on the system in the process of system modeling and controller design, and a controller is designed to take into account the uncertain factors based on incomplete information about uncertainty, so that the actual system can meet the expected performance index. Specifically, this paper proposes an optimal nonlinear robust sliding mode control (ONRSMC) based on mixed $\mathcal{H}_2/\mathcal{H}_\infty$ linear matrix inequalities (LMIs) for excitation control of a one machine-infinite bus system (OMIBS). The chaos mapping-based adaptive salp swarm algorithm (CASSA) algorithm is used to optimize the parameters of ONRSMC, thereby introducing an intelligent ONRSMC. Simulation results show that the proposed method is effective in damping voltage oscillations under severe disturbances and uncertainties. The main innovations of this paper can be summarized as:

1) An ONRSMC for excitation control is designed, which integrates mixed $\mathcal{H}_2/\mathcal{H}_\infty$ LMIs in the control design and sliding surface to ensure mixed robustness.

2) By applying the CASSA algorithm to optimize and adjust parameters, an intelligent ONRSMC for excitation control is introduced.

3) Voltage oscillations caused by disturbances and uncertainties in the OMIBS are suppressed, while the system's robustness with different controllers and parameter perturbations are also investigated.

The organization of the rest of the paper is as follows. Section II introduces the nonlinear mathematical model of the OMIBS and its corresponding feedback linearization mathematical model. In Section III, an ONRSMC is designed for the OMIBS, while Section IV proposes the CASSA algorithm and its application in optimizing ONRSMC. Section V presents simulation studies to demonstrate the advantages of the new method. Section VI concludes the paper.

II. System Mathematical Models

A. OMIBS Modeling

The OMIBS is illustrated in Fig. 1. From [1], the system model depicted can be described by the rotor motion equation of the generator and the electromagnetic dynamic equation of the rotor winding as:

$$\begin{cases} \dot{\delta} = \omega - \omega_0 \\ \dot{\omega} = -\dfrac{D}{H}(\omega - \omega_0) - \dfrac{\omega_0}{H}(P_\mathrm{e} - P_\mathrm{m}) \\ \dot{E}'_q = -\dfrac{1}{T'_d}E'_q + \dfrac{1}{T_{d0}}\dfrac{x_d - x'_d}{x'_{d\Sigma}}V_\mathrm{s}\cos\delta + \dfrac{1}{T_{d0}}V_f \\ P_\mathrm{e} = \dfrac{E'_q V_\mathrm{s}}{x'_{d\Sigma}}\sin\delta + \dfrac{V_\mathrm{s}^2}{2}\left(\dfrac{x'_d - x_q}{x'_{d\Sigma}x_{q\Sigma}}\right)\sin 2\delta \end{cases} \tag{1}$$

where δ is the rotor angle; ω is the speed; ω_0 is the initial values of ω; D is the damping coefficient; H is the inertia constant; P_m is the mechanical power input; P_e is the generator electromagnetic power; E'_q is the quadrature q-axis transient voltage; V_s is the infinite bus voltage; while $x'_{d\Sigma} = x'_d + x_\mathrm{T} + x_\mathrm{L}$ and $x_{q\Sigma} = x_q + x_\mathrm{T} + x_\mathrm{L}$ are the reactance sum of the d-axis and q-axis, respectively; x_d is the d-axis synchronous reactance; x'_d is the d-axis transient reactance; x_q is the q-axis reactance; x_T is the reactance of the transformer; x_L is the reactance of the transmission line; T_{d0} is the excitation winding time constant; T'_d is the d-axis transient time constant; and V_f is the excitation control input.

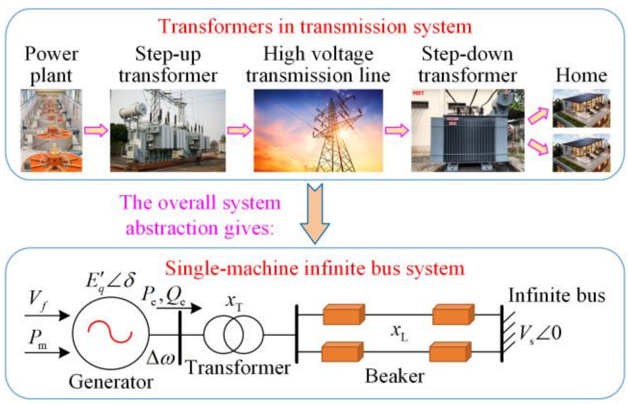

Fig. 1. A one machine-infinite bus power system.

B. Direct Feedback Linearization Modeling

Before carrying out feedback linearization modeling, we make two assumptions: 1) The mechanical power of the synchronous generator remains constant, i.e., $P_\mathrm{m} = P_\mathrm{m0} = P_\mathrm{e0}$; and 2) The voltage V_s of the OMIBS remains constant. Then, the first-order derivative of the electromagnetic power P_e of the generator is obtained as:

$$\begin{aligned}\dot{P}_{\mathrm{e}} &= \frac{V_{\mathrm{s}}}{x'_{d\Sigma}}(\dot{E}_q \sin\delta + \dot{\delta}E'_q\cos\delta) + \dot{\delta}\frac{V_{\mathrm{s}}^2(x'_d - x_q)}{x'_{d\Sigma}x_{q\Sigma}}\cos 2\delta = \\ &\frac{V_{\mathrm{s}}}{x'_{d\Sigma}}\left[\begin{array}{l} E'_q(\omega-\omega_0)\cos\delta + \\ \left(\begin{array}{l} -\dfrac{1}{T'_d}E'_q + \\ \dfrac{1}{T_{d0}}\dfrac{x_d - x'_d}{x'_{d\Sigma}}V_{\mathrm{s}}\cos\delta + \dfrac{1}{T_{d0}}V_f \end{array}\right)\sin\delta \end{array}\right] + \\ &V_{\mathrm{s}}^2\left(\frac{x'_d - x_q}{x'_{d\Sigma}x_{q\Sigma}}\right)(\omega-\omega_0)\cos 2\delta \end{aligned} \tag{2}$$

The rotor angle, speed, and the electromagnetic power deviations are defined as:

$$\begin{cases} \Delta\delta = \delta - \delta_0 \\ \Delta\omega = \omega - \omega_0 \\ \Delta P_{\mathrm{e}} = P_{\mathrm{e}} - P_{\mathrm{e0}} \end{cases} \tag{3}$$

where δ_0 and P_{e0} denote the initial values of the respective variables.

Based on the derivative calculation result of (2) and using the direct feedback linearization method, a virtual control input is defined as $u = (\omega_0 / H)\dot{P}_{\mathrm{e}}$. By combining with (1), a linear state-space differential equation can be derived as:

$$\dot{\boldsymbol{x}}' = \boldsymbol{A}'\boldsymbol{x}' + \boldsymbol{B}'_1\boldsymbol{u} \tag{4}$$

where

$$\begin{cases} \boldsymbol{x}' = [\Delta\delta \quad \Delta\omega \quad \Delta P_{\mathrm{e}}]^{\mathrm{T}} \\ \boldsymbol{B}'_1 = \begin{bmatrix} 0 & 0 & \dfrac{H}{\omega_0} \end{bmatrix}^{\mathrm{T}} \\ \boldsymbol{A}' = \begin{bmatrix} 0 & 1 & 0 \\ 0 & -\dfrac{D}{H} & -\dfrac{\omega_0}{H} \\ 0 & 0 & 0 \end{bmatrix} \end{cases} \tag{5}$$

In order to achieve sufficient accuracy in voltage regulation of the excitation system and eliminate the steady-state error of the generator terminal voltage, the integrated value of the terminal voltage deviation is introduced as a state variable, described as:

$$V_{\mathrm{int}} = \int \Delta V_{\mathrm{t}}\mathrm{d}t = \int (V_{\mathrm{t}} - V_{\mathrm{t0}})\mathrm{d}t \tag{6}$$

where V_{t} is the generator terminal voltage and V_{t0} is the generator rated terminal voltage.

Since the issue of voltage accuracy control can be discussed within a small-range near the operating point, a small range linearization can be applied. It can be derived that there is a relationship between the deviation of electromagnetic power ΔP_{e}, rotor angle deviation $\Delta\delta$, and terminal voltage deviation ΔV_{t}, as:

$$\Delta P_{\mathrm{e}} = S_{\mathrm{v}}\Delta\delta + R_{\mathrm{v}}\Delta V_{\mathrm{t}} \tag{7}$$

$$\begin{cases} S_{\mathrm{v}} = S_{\mathrm{E}} - R_{\mathrm{v}}\dfrac{\partial V_{\mathrm{t}}}{\partial\delta} \\ R_{\mathrm{v}} = \dfrac{R_{\mathrm{E}}}{\dfrac{\partial V_{\mathrm{t}}}{\partial E_q}} \end{cases} \tag{8}$$

where

$$\begin{cases} S_{\mathrm{E}} = \dfrac{E_q V_{\mathrm{s}}}{x_{d\Sigma}}\cos\delta + V_{\mathrm{s}}^2\left(\dfrac{x'_d - x_q}{x'_{d\Sigma}x_{q\Sigma}}\right)\cos 2\delta \\ R_{\mathrm{E}} = \dfrac{V_{\mathrm{s}}}{x_{d\Sigma}}\sin\delta \\ \dfrac{\partial V_t}{\partial\delta} = \dfrac{1}{2}\left(\dfrac{V_{\mathrm{s}}^2 x_q^2\sin 2\delta}{x_{q\Sigma}^2} - \dfrac{V_{\mathrm{s}}^2 x_d^2\sin 2\delta + 2x_{\mathrm{s}}x_d E_q V_{\mathrm{s}}\sin\delta}{x_{d\Sigma}^2}\right)\times \\ \left(\begin{array}{l}\dfrac{E_q^2 x_{\mathrm{s}}^2 + V_{\mathrm{s}}^2\cos^2\delta x_d^2 + 2x_{\mathrm{s}}x_d E_q V_{\mathrm{s}}\cos\delta}{x_{d\Sigma}^2} + \\ \dfrac{V_{\mathrm{s}}^2\sin^2\delta x_q^2}{x_{q\Sigma}^2}\end{array}\right)^{-0.5} \\ \dfrac{\partial V_t}{\partial E_q} = \left(\dfrac{E_q x_{\mathrm{s}}^2 + x_{\mathrm{s}}x_d V_{\mathrm{s}}\cos\delta}{x_{d\Sigma}^2}\right)\times \\ \left(\begin{array}{l}\dfrac{E_q^2 x_{\mathrm{s}}^2 + V_{\mathrm{s}}^2\cos^2\delta x_d^2 + 2x_{\mathrm{s}}x_d E_q V_{\mathrm{s}}\cos\delta}{x_{d\Sigma}^2} + \\ \dfrac{V_{\mathrm{s}}^2\sin^2\delta x_q^2}{x_{q\Sigma}^2}\end{array}\right)^{-0.5} \end{cases} \tag{9}$$

The impedance x_{s} mentioned above is defined as (10), and the open-circuit voltage on the q-axis of the generator is as (11):

$$x_{\mathrm{s}} = x_t + x_{\mathrm{L}} \tag{10}$$

$$E_q = E'_q + \frac{E'_q - V_{\mathrm{s}}\cos\delta}{x'_{d\Sigma}}(x_d - x'_d) \tag{11}$$

Using the relationship described in (6) and (7), the derivative of V_{int} can be expressed mathematically as:

$$\dot{V}_{\mathrm{int}} = \Delta V_{\mathrm{t}} = -\frac{S_{\mathrm{v}}}{R_{\mathrm{v}}}\Delta\delta + \frac{1}{R_{\mathrm{v}}}\Delta P_{\mathrm{e}} \tag{12}$$

Finally, by combining (4) and (12), the feedback linearization model for the OMIBS is obtained as:

$$\dot{\boldsymbol{x}} = \boldsymbol{A}\boldsymbol{x} + \boldsymbol{B}_1\boldsymbol{u} \tag{13}$$

where

$$\begin{cases} \boldsymbol{x} = [\Delta\delta \quad \Delta\omega \quad \Delta P_{\mathrm{e}} \quad V_{\mathrm{int}}]^{\mathrm{T}} \\ \boldsymbol{B}_1 = \begin{bmatrix} 0 & 0 & \dfrac{H}{\omega_0} & 0 \end{bmatrix}^{\mathrm{T}} \\ \boldsymbol{A} = \begin{bmatrix} 0 & 1 & 0 & 0 \\ 0 & -\dfrac{D}{H} & -\dfrac{\omega_0}{H} & 0 \\ 0 & 0 & 0 & 0 \\ -\dfrac{S_{\mathrm{v}}}{R_{\mathrm{v}}} & 0 & \dfrac{1}{R_{\mathrm{v}}} & 0 \end{bmatrix} \end{cases} \tag{14}$$

However, in actual power systems, parameters such as system damping coefficient D, inertia time constant H, and line reactance x_L are often difficult to measure or estimate accurately. On the other hand, there are often external disturbances, such as changes in operating conditions and various faults in the system. Therefore, it is necessary to establish a mathematical model that includes the above uncertain factors based on the system described in (13). In this paper, considering parameter deviations of $\Delta D, \Delta H, \Delta S_v, \Delta R_v$, and external disturbances of w_1 , w_2 , and w_3 , the OMIBS can be described as follows:

$$\dot{\boldsymbol{x}} = (\boldsymbol{A} + \Delta \boldsymbol{A})x + (\boldsymbol{B}_1 + \Delta \boldsymbol{B}_1)\boldsymbol{u} + \boldsymbol{B}_2 \boldsymbol{w} \tag{15}$$

where $\boldsymbol{w}$ is the disturbance vector and $\| \boldsymbol{w} \| \leqslant \delta_f$; $\boldsymbol{B}_1$, $\Delta \boldsymbol{B}_1$, $\boldsymbol{B}_2$ and $\Delta \boldsymbol{A}$ can be expressed as follows:

$$\begin{cases} \boldsymbol{B}_1 = \begin{bmatrix} 0 & 0 & \dfrac{H}{\omega_0} & 0 \end{bmatrix}^{\mathrm{T}} \\ \Delta \boldsymbol{B}_1 = \begin{bmatrix} 0 & 0 & \dfrac{\Delta H}{\omega_0} & 0 \end{bmatrix}^{\mathrm{T}} \\ \boldsymbol{B}_2 = \begin{bmatrix} 0 & d_1 & d_2 & d_3 \end{bmatrix}^{\mathrm{T}} \\ \Delta \boldsymbol{A} = \begin{bmatrix} 0 & 0 & 0 & 0 \\ 0 & \dfrac{D\Delta H - H\Delta D}{H(H+\Delta H)} & \dfrac{\omega_0 \Delta H}{H(H+\Delta H)} & 0 \\ 0 & 0 & 0 & 0 \\ \dfrac{S_v \Delta R_v - R_v \Delta S_v}{R_v(R_v + \Delta R_v)} & 0 & \dfrac{\Delta R_v}{R_v(R_v+\Delta R_v)} & 0 \end{bmatrix} \end{cases} \tag{16}$$

From robust control theory, for controlled object systems with uncertain factors, the perturbation matrices $\Delta \boldsymbol{A}$ and $\Delta \boldsymbol{B}_1$ in (15) should satisfy the relevant matching conditions. The parameter uncertainties $\Delta \boldsymbol{A}$ and $\Delta \boldsymbol{B}_1$ are in the following form:

$$[\Delta \boldsymbol{A} \quad \Delta \boldsymbol{B}_1] = \boldsymbol{H}_c \boldsymbol{F} [\boldsymbol{E}_a \quad \boldsymbol{E}_b] \tag{17}$$

where $\boldsymbol{H}_c \in \mathbb{R}^{4\times4}$, $\boldsymbol{E}_a \in \mathbb{R}^{4\times4}$ and $\boldsymbol{E}_b \in \mathbb{R}^{4\times1}$ are known constant matrices of appropriate dimensions; $\boldsymbol{F} \in \mathbb{R}^{4\times4}$ is an unknown real matrix containing the uncertainty, which satisfies $\boldsymbol{F}^{\mathrm{T}}\boldsymbol{F} \leqslant \boldsymbol{I}$, and $\boldsymbol{I}$ is an identity matrix.

III. Design of Controller

A. Sliding Mode Control Based on the Equivalent Principle

The sliding surface for the system given in (15) can be considered as:

$$\boldsymbol{S} = (\boldsymbol{B}_1 + \boldsymbol{H}_c \boldsymbol{E}_b)^{\mathrm{T}} \boldsymbol{P} \boldsymbol{x} \tag{18}$$

where $\boldsymbol{P}$ is a positive definite matrix to be determined.

Based on (18), the mathematical expression of the designed sliding mode control (SMC) is described as:

$$\boldsymbol{u} = \boldsymbol{u}_{eq} + \boldsymbol{u}_n \tag{19}$$

The controller (19) consists of two parts: 1) equivalent control term $\boldsymbol{u}_{eq}$, which ensures that the system satisfies the sliding mode reaching condition from any state; and 2) robust control term $\boldsymbol{u}_n$, which ensures that the uncertain sliding mode control system maintains good performance with internal parameter perturbations and external disturbances.

From the principle of equivalent control and defining $\boldsymbol{w} = 0$, we can obtain from the system with uncertainty described by (15) and $\dot{\boldsymbol{S}} = 0$, that:

$$\begin{aligned} \dot{\boldsymbol{S}} &= (\boldsymbol{B}_1 + \boldsymbol{H}_c \boldsymbol{E}_b)^{\mathrm{T}} \boldsymbol{P} \dot{\boldsymbol{x}} = (\boldsymbol{B}_1 + \boldsymbol{H}_c \boldsymbol{E}_b)^{\mathrm{T}} \boldsymbol{P} \times \\ &(\boldsymbol{A}\boldsymbol{x} + \Delta \boldsymbol{A}\boldsymbol{x} + \boldsymbol{B}_1 \boldsymbol{u} + \Delta \boldsymbol{B}_1 \boldsymbol{u}) = 0 \end{aligned} \tag{20}$$

Combining with the analysis of the uncertainty matrix described in (17), the expression for the equivalent control term $\boldsymbol{u}_{eq}$ can be obtained:

$$\begin{aligned} \boldsymbol{u}_{eq} &= -[(\boldsymbol{B}_1 + \boldsymbol{H}_c \boldsymbol{E}_b)^{\mathrm{T}} \boldsymbol{P} (\boldsymbol{B}_1 + \boldsymbol{H}_c \boldsymbol{E}_b)]^{-1} \times \\ &(\boldsymbol{B}_1 + \boldsymbol{H}_c \boldsymbol{E}_b)^{\mathrm{T}} \boldsymbol{P} (\boldsymbol{A} + \boldsymbol{H}_c \boldsymbol{E}_a) \boldsymbol{x} \end{aligned} \tag{21}$$

To ensure $\dot{\boldsymbol{S}}\boldsymbol{S} < 0$, the robust control term $\boldsymbol{u}_n$ in the SMC in this paper is defined as:

$$\begin{aligned} \boldsymbol{u}_n &= -[(\boldsymbol{B}_1 + \boldsymbol{H}_c \boldsymbol{E}_b)^{\mathrm{T}} \boldsymbol{P} (\boldsymbol{B}_1 + \boldsymbol{H}_c \boldsymbol{E}_b)]^{-1} \times \\ &(\| (\boldsymbol{B}_1 + \boldsymbol{H}_c \boldsymbol{E}_b)^{\mathrm{T}} \boldsymbol{P} \boldsymbol{B}_2 \| \delta_f + \varepsilon_0) \operatorname{sgn}(\boldsymbol{S}) \end{aligned} \tag{22}$$

where ε_0 is a small normal number.

The Lyapunov function used for stability proof is defined as:

$$V = \frac{1}{2} \boldsymbol{S}^{\mathrm{T}} \boldsymbol{S} \tag{23}$$

Clearly, for all $\boldsymbol{S}(\boldsymbol{x},t) \neq 0$, the Lyapunov function V is positive definite. Differentiating (23) with respect to (15) yields:

$$\begin{aligned} \dot{V} &= \boldsymbol{S}^{\mathrm{T}} \dot{\boldsymbol{S}} = \boldsymbol{S}^{\mathrm{T}} (\boldsymbol{B}_1 + \boldsymbol{H}_c \boldsymbol{E}_b)^{\mathrm{T}} \boldsymbol{P} \dot{\boldsymbol{x}} = \\ &\boldsymbol{S}^{\mathrm{T}} \left\{ (\boldsymbol{B}_1 + \boldsymbol{H}_c \boldsymbol{E}_b)^{\mathrm{T}} \boldsymbol{P} [(\boldsymbol{A} + \Delta \boldsymbol{A}) \boldsymbol{x} + (\boldsymbol{B}_1 + \Delta \boldsymbol{B}_1) \boldsymbol{u} + \right. \\ &\left. \boldsymbol{B}_2 \boldsymbol{w}] \right\} = \boldsymbol{S}^{\mathrm{T}} [(\boldsymbol{B}_1 + \boldsymbol{H}_c \boldsymbol{E}_b)^{\mathrm{T}} \boldsymbol{P} (\boldsymbol{B}_1 + \boldsymbol{H}_c \boldsymbol{E}_b) \boldsymbol{u}_n + \\ &(\boldsymbol{B}_1 + \boldsymbol{H}_c \boldsymbol{E}_b)^{\mathrm{T}} \boldsymbol{P} \boldsymbol{B}_2 w] = \\ &- \boldsymbol{S}^{\mathrm{T}} [\| (\boldsymbol{B}_1 + \boldsymbol{H}_c \boldsymbol{E}_b)^{\mathrm{T}} \boldsymbol{P} \boldsymbol{B}_2 \| \delta_f + \varepsilon_0] \operatorname{sgn}(s) + \\ &\boldsymbol{S}^{\mathrm{T}} (\boldsymbol{B}_1 + \boldsymbol{H}_c \boldsymbol{E}_b)^{\mathrm{T}} \boldsymbol{P} \boldsymbol{B}_2 \boldsymbol{w} \leqslant \\ &\| \boldsymbol{S} \| \| (\boldsymbol{B}_1 + \boldsymbol{H}_c \boldsymbol{E}_b)^{\mathrm{T}} \boldsymbol{P} \boldsymbol{B}_2 \| \delta_f - \\ &\boldsymbol{S}^{\mathrm{T}} (\| (\boldsymbol{B}_1 + \boldsymbol{H}_c \boldsymbol{E}_b)^{\mathrm{T}} \boldsymbol{P} \boldsymbol{B}_2 \| \delta_f + \varepsilon_0) \operatorname{sgn}(\boldsymbol{S}) \leqslant \\ &- \varepsilon_0 \| \boldsymbol{S} \| \leqslant 0 \end{aligned} \tag{24}$$

Based on the above derivation, the following result can be obtained:

$$\dot{V} \leqslant 0 \tag{25}$$

Equation (25) shows that the system from any initial state satisfies the sliding mode arrival condition.

The next step is to design a sliding surface that satisfies mixed robustness performance, allowing the sliding mode control system to maintain robust performance in various disturbance conditions.

B. SMC Analysis and Matrix Design

In this section, the method of auxiliary feedback is used to introduce the mixed $\mathcal{H}_2/\mathcal{H}_\infty$ LMIs to design the positive definite matrix $\boldsymbol{P}$ in the sliding mode surface and to ensure good robustness of the SMC with internal parameter perturbations and external disturbances. First, the mathematical description of the controller described by (19) is rewritten in the form of virtual state feedback, expressed mathematically as:

$$\boldsymbol{u}=\boldsymbol{K}\boldsymbol{x}+\boldsymbol{v} \tag{26}$$

where $\boldsymbol{v}=-\boldsymbol{K}\boldsymbol{x}+\boldsymbol{u}_{\mathrm{eq}}+\boldsymbol{u}_{\mathrm{n}}$ and $\boldsymbol{K}$ is the state feedback matrix.

Based on the feedback form described by (26), the entire closed-loop system can be represented as:

$$\dot{\boldsymbol{x}}=[(\boldsymbol{A}+\Delta\boldsymbol{A})+(\boldsymbol{B}_1+\Delta\boldsymbol{B}_1)\boldsymbol{K}]\boldsymbol{x}+\boldsymbol{B}_\Sigma\boldsymbol{w}_\Sigma \tag{27}$$

where $\boldsymbol{B}_\Sigma=[\boldsymbol{B}_1+\Delta\boldsymbol{B}_1 \quad \boldsymbol{B}_2]$, and $\boldsymbol{w}_\Sigma=[\boldsymbol{v} \quad \boldsymbol{w}]^{\mathrm{T}}$.

Then, combining the closed-loop system described by (27) with its mixed $\mathcal{H}_2/\mathcal{H}_\infty$ control performance output vectors $\boldsymbol{z}_\infty$ and $\boldsymbol{z}_2$, the augmented mathematical model is obtained:

$$\begin{cases}\dot{\boldsymbol{x}}=[(\boldsymbol{A}+\Delta\boldsymbol{A})+(\boldsymbol{B}_1+\Delta\boldsymbol{B}_1)\boldsymbol{K}]\boldsymbol{x}+\boldsymbol{B}_\Sigma\boldsymbol{w}_\Sigma\\ \boldsymbol{z}_\infty=(\boldsymbol{C}_\infty+\boldsymbol{D}_{\infty1}\boldsymbol{K})\boldsymbol{x}+\boldsymbol{D}_{\infty2}\boldsymbol{w}_\Sigma\\ \boldsymbol{z}_2=(\boldsymbol{C}_2+\boldsymbol{D}_{21}\boldsymbol{K})\boldsymbol{x}\end{cases} \tag{28}$$

where $\boldsymbol{z}_\infty\in\mathbb{R}^5$ and $\boldsymbol{z}_2\in\mathbb{R}^5$ are performance matrices. The matrices in (28) are defined as:

$$\begin{cases}\boldsymbol{C}_\infty=[\boldsymbol{Q}_\infty \quad 0]^{\mathrm{T}}\\ \boldsymbol{D}_{\infty1}=[0 \quad \boldsymbol{R}_\infty]^{\mathrm{T}}\\ \boldsymbol{D}_{\infty2}=0\\ \boldsymbol{C}_2=[\boldsymbol{Q}_2 \quad 0]^{\mathrm{T}}\\ \boldsymbol{D}_{21}=[0 \quad \boldsymbol{R}_2]^{\mathrm{T}}\end{cases} \tag{29}$$

where $\boldsymbol{R}_2\in\mathbb{R}^{1\times1}$, $\boldsymbol{Q}_2\in\mathbb{R}^{4\times4}$ and $\boldsymbol{R}_\infty\in\mathbb{R}^{1\times1}$, $\boldsymbol{Q}_\infty\in\mathbb{R}^{4\times4}$ are real constant matrices to be determined. The structures of the matrices $\boldsymbol{R}_2$, $\boldsymbol{Q}_2$, $\boldsymbol{R}_\infty$, and $\boldsymbol{Q}_\infty$ are defined as:

$$\begin{cases}\boldsymbol{Q}_\infty=\mathrm{diag}\,(q_{11},q_{12},q_{13},q_{14})\\ \boldsymbol{Q}_2=\mathrm{diag}\,(q_{21},q_{22},q_{23},q_{24})\\ \boldsymbol{R}_\infty=r_1\\ \boldsymbol{R}_2=r\end{cases} \tag{30}$$

where $q_{ij}, r_i>0\ (i=1,2; j=1,2,3,4)$ are weighting factors.

Corresponding to the two output vectors $\boldsymbol{z}_\infty$ and $\boldsymbol{z}_2$, the transfer function matrices are given respectively by:

$$\begin{gathered}\boldsymbol{G}_{z_\infty w_\Sigma}(s)=(\boldsymbol{C}_\infty+\boldsymbol{D}_{\infty1}\boldsymbol{K})\times\\ (s\boldsymbol{I}-[(\boldsymbol{A}+\Delta\boldsymbol{A})+(\boldsymbol{B}_1+\Delta\boldsymbol{B}_1)\boldsymbol{K}])^{-1}\boldsymbol{B}_2+\boldsymbol{D}_{\infty2}\end{gathered} \tag{31}$$

$$\begin{gathered}\boldsymbol{G}_{z_2 w_\Sigma}(s)=(\boldsymbol{C}_2+\boldsymbol{D}_{21}\boldsymbol{K})\times\\ (s\boldsymbol{I}-[(\boldsymbol{A}+\Delta\boldsymbol{A})+(\boldsymbol{B}_1+\Delta\boldsymbol{B}_1)\boldsymbol{K}])^{-1}\boldsymbol{B}_2\end{gathered} \tag{32}$$

Thus, the $\mathcal{H}_\infty$ performance and $\mathcal{H}_2$ performance requirements are respectively given as:

$$\|\boldsymbol{G}_{z_\infty w_\Sigma}(s)\|_\infty<\gamma_\infty \tag{33}$$

$$\|\boldsymbol{G}_{z_2 w_\Sigma}(s)\|_2<\gamma_2 \tag{34}$$

where $\gamma_\infty>0$ and $\gamma_2>0$.

The design objective of mixed $\mathcal{H}_2/\mathcal{H}_\infty$ control is to design a state feedback control law for the linear system expressed in (28) such that it satisfies $\mathcal{H}_\infty$ performance (33) and $\mathcal{H}_2$ performance (34).

1) $\mathcal{H}_\infty$ Control Performance

$\mathcal{H}_\infty$ control performance (33) is met if and only if there exist a scalar α, a matrix $\boldsymbol{W}_\infty$, and $\boldsymbol{X}_\infty>0$, such that:

$$\begin{bmatrix}\Psi_{\infty1}(\boldsymbol{X}_\infty,\boldsymbol{W}_\infty) & \boldsymbol{B}_2 & * & *\\ \boldsymbol{B}_2^{\mathrm{T}} & -\gamma_\infty\boldsymbol{I} & * & *\\ \Psi_{\infty2}(\boldsymbol{X}_\infty,\boldsymbol{W}_\infty) & D_{\infty2} & -\gamma_\infty\boldsymbol{I} & *\\ \Psi_{\infty3}(\boldsymbol{X}_\infty,\boldsymbol{W}_\infty) & 0 & 0 & -\alpha\boldsymbol{I}\end{bmatrix}<0 \tag{35}$$

where the symbol "*" denotes matrix blocks obtained from the symmetry of the matrix and there are:

$$\begin{cases}\Psi_{\infty1}(\boldsymbol{X}_\infty,\boldsymbol{W}_\infty)=(\boldsymbol{A}\boldsymbol{X}_\infty+\boldsymbol{B}_1\boldsymbol{W}_\infty)+(\boldsymbol{A}\boldsymbol{X}_\infty+\boldsymbol{B}_1\boldsymbol{W}_\infty)^{\mathrm{T}}+\\ \qquad\qquad \alpha\boldsymbol{H}_{\mathrm{c}}\boldsymbol{H}_{\mathrm{c}}^{\mathrm{T}}\\ \Psi_{\infty2}(\boldsymbol{X}_\infty,\boldsymbol{W}_\infty)=\boldsymbol{C}_\infty\boldsymbol{X}_\infty+\boldsymbol{D}_{\infty1}\boldsymbol{W}_\infty\\ \Psi_{\infty3}(\boldsymbol{X}_\infty,\boldsymbol{W}_\infty)=\boldsymbol{E}_a\boldsymbol{X}_\infty+\boldsymbol{E}_{\mathrm{b}}\boldsymbol{W}_\infty\end{cases} \tag{36}$$

When the LMI condition of (35) is met, the feedback gain can be taken as $\boldsymbol{K}=\boldsymbol{K}_\infty=\boldsymbol{W}_\infty\boldsymbol{P}_\infty=\boldsymbol{W}_\infty\boldsymbol{X}_\infty^{-1}$. Therefore, from the results here, it is known that only if the sliding mode of the designed SMC system has $\mathcal{H}_\infty$ performance, can the parameters in the sliding surface (18) be $\boldsymbol{P}=\boldsymbol{P}_\infty=\boldsymbol{X}_\infty^{-1}$.

2) $\mathcal{H}_2$ Control Performance

$\mathcal{H}_2$ control performance (34) is met if and only if there exist a scalar β, a matrix $\boldsymbol{W}_2$, and two symmetric matrices $\boldsymbol{Z}$ and $\boldsymbol{X}_2$, such that:

$$\begin{cases}\begin{bmatrix}\Phi_{21}(\boldsymbol{X}_2,\boldsymbol{W}_2) & *\\ \Phi_{22}(\boldsymbol{X}_2,\boldsymbol{W}_2) & -\beta\boldsymbol{I}\end{bmatrix}<0\\ \begin{bmatrix}-\boldsymbol{Z} & *\\ \Phi_{32}(\boldsymbol{X}_2,\boldsymbol{W}_2) & -\boldsymbol{X}_2\end{bmatrix}<0\\ \mathrm{trace}(\boldsymbol{Z})<\gamma_2^2\end{cases} \tag{37}$$

where

$$\begin{cases}\Phi_{21}(\boldsymbol{X}_2,\boldsymbol{W}_2)=(\boldsymbol{A}\boldsymbol{X}_2+\boldsymbol{B}_1\boldsymbol{W}_2)+(\boldsymbol{A}\boldsymbol{X}_2+\boldsymbol{B}_1\boldsymbol{W}_2)^{\mathrm{T}}+\\ \qquad\qquad \boldsymbol{B}_2\boldsymbol{B}_2^{\mathrm{T}}+\beta\boldsymbol{H}_{\mathrm{c}}\boldsymbol{H}_{\mathrm{c}}^{\mathrm{T}}\\ \Phi_{22}(\boldsymbol{X}_2,\boldsymbol{W}_2)=\boldsymbol{E}_{\mathrm{a}}\boldsymbol{X}_2+\boldsymbol{E}_{\mathrm{b}}\boldsymbol{W}_2\\ \Phi_{32}(\boldsymbol{X}_2,\boldsymbol{W}_2)=(\boldsymbol{C}_2\boldsymbol{X}_2+\boldsymbol{D}_{21}\boldsymbol{W}_2)^{\mathrm{T}}\end{cases} \tag{38}$$

When the condition of (37) is met, the feedback gain can be taken as $\boldsymbol{K}=\boldsymbol{K}_2=\boldsymbol{W}_2\boldsymbol{P}_2=\boldsymbol{W}_2\boldsymbol{X}_2^{-1}$. Similarly, only if the sliding mode of the designed SMC system has $\mathcal{H}_2$ performance, can the sliding surface (18) parameters be $\boldsymbol{P}_2=\boldsymbol{X}_2^{-1}$.

3) $\mathcal{H}_2/\mathcal{H}_\infty$ Performance

In order for the feedback controller to possess both $\mathcal{H}_2$ and $\mathcal{H}_\infty$ control performances, two sets are defined based on the conditions of the two LMIs (35) and (37):

$$\begin{cases}\boldsymbol{\Pi}_\infty=\{(\boldsymbol{X}_\infty,\boldsymbol{W}_\infty)|\ \boldsymbol{X}_\infty>0,\boldsymbol{W}_\infty\in\mathbb{R}^{4\times5},\\ \qquad \exists\alpha>0,\text{ s.t. (35) holds}\},\\ \boldsymbol{\Pi}_2=\{(\boldsymbol{X}_2,\boldsymbol{W}_2)|\ \boldsymbol{X}_2>0,\boldsymbol{W}_2\in\mathbb{R}^{1\times4},\\ \qquad \exists\beta>0,Z\in\mathbb{S}^4,\text{ s.t. (37) holds}\}\end{cases}\tag{39}$$

Additionally, here $\boldsymbol{\Pi}_2$ is used to represent the intersection of $\boldsymbol{\Pi}_\infty$ and $\boldsymbol{\Pi}_2$, i.e.:

$$\boldsymbol{\Pi}_0=\boldsymbol{\Pi}_\infty\cap\boldsymbol{\Pi}_2\tag{40}$$

Given that the problem is to find a single feedback gain $\boldsymbol{K}$ that satisfies both requirements in (35) and (37) simultaneously, considering the two expressions for the gain matrix $\boldsymbol{K}$, it is evident that there is a clear connection between the two in (35) and (37), i.e.:

$$\boldsymbol{W}_\infty\boldsymbol{X}_\infty^{-1}=\boldsymbol{W}_2\boldsymbol{X}_2^{-1}\tag{41}$$

$\mathcal{H}_2/\mathcal{H}_\infty$ performance has a solution if and only if the following parameter set (42) is not null.

$$\mathbb{F}=\left\{(\boldsymbol{X}_\infty,\boldsymbol{W}_\infty,\boldsymbol{X}_2,\boldsymbol{W}_2)\left|\begin{array}{l}\begin{cases}(\boldsymbol{X}_\infty,\boldsymbol{W}_\infty)\in\Pi_\infty\\(\boldsymbol{X}_2,\boldsymbol{W}_2)\in\Pi_2\end{cases}\\ \boldsymbol{W}_\infty\boldsymbol{X}_\infty^{-1}=\boldsymbol{W}_2\boldsymbol{X}_2^{-1}\end{array}\right.\right\}\tag{42}$$

And in this case, a feedback gain is given by $\boldsymbol{K}=\boldsymbol{W}_\infty\boldsymbol{X}_\infty^{-1}=\boldsymbol{W}_2\boldsymbol{X}_2^{-1}$.

It can be seen from (42) that finding $(\boldsymbol{X}_\infty,\boldsymbol{W}_\infty,\boldsymbol{X}_2,\boldsymbol{W}_2)\in\mathbb{F}$ is not an LMI problem, as (42) involves the definition of the parameter set $\mathbb{F}$ we set $\boldsymbol{W}_\infty=\boldsymbol{W}_2\triangleq\boldsymbol{W}$. Then, the parameter set $\mathbb{F}$ reduces to:

$$\mathbb{F}_0=\{(\boldsymbol{X},\boldsymbol{W},\boldsymbol{X},\boldsymbol{W})|(\boldsymbol{X},\boldsymbol{W})\in\Pi_0\}\tag{43}$$

Therefore, to avoid the difficulties, we may find a $(\boldsymbol{X},\boldsymbol{W})\in\Pi_0$ instead of a $(\boldsymbol{X}_\infty,\boldsymbol{W}_\infty,\boldsymbol{X}_2,\boldsymbol{W}_2)\in\mathbb{F}$, and the feedback gain matrix is computed by:

$$\boldsymbol{K}=\boldsymbol{W}\boldsymbol{P}=\boldsymbol{W}\boldsymbol{X}^{-1}\tag{44}$$

where matrix $\boldsymbol{P}$ is the same as in the sliding mode surface in (18), and $\boldsymbol{W}$ is a coefficient matrix. In addition, through the definition of matrix $\boldsymbol{K}$ and sliding mode surface $\boldsymbol{S}$, it can be found that: 1) from the matrix structure, both have the same structural form; 2) from the feedback function, both matrix $\boldsymbol{P}$ play the role of feedback information fusion; and 3) both corresponding control functions need the computational solution of matrix $\boldsymbol{P}$. Therefore, equations (35) and (37) are used to complete the mixed $\mathcal{H}_2/\mathcal{H}_\infty$ controller performance design and obtain the required matrix P in the sliding mode surface. The mixed $\mathcal{H}_2/\mathcal{H}_\infty$ controller performance has a solution if there exist scalars a, β, two symmetric matrices $\boldsymbol{P}=\boldsymbol{X}^{-1}$, $\boldsymbol{Z}$, and a matrix $\boldsymbol{W}$, satisfying the following optimization problem:

$$\min\{c_2\gamma_2+c_\infty\gamma_\infty\},$$
$$\text{s.t.}\begin{cases}\begin{bmatrix}\Psi_1(\boldsymbol{X},\boldsymbol{W}) & * & * & *\\ \boldsymbol{B}_2^{\mathrm{T}} & -\gamma_\infty\boldsymbol{I} & * & *\\ \Psi_2(\boldsymbol{X},\boldsymbol{W}) & \boldsymbol{D}_{\infty2} & -\gamma_\infty\boldsymbol{I} & *\\ \Psi_3(\boldsymbol{X},\boldsymbol{W}) & \boldsymbol{0} & \boldsymbol{0} & -\alpha\boldsymbol{I}\end{bmatrix}<\boldsymbol{0}\\ \begin{bmatrix}\Phi_1(\boldsymbol{X},\boldsymbol{W}) & *\\ \Phi_2(\boldsymbol{X},\boldsymbol{W}) & -\beta\boldsymbol{I}\end{bmatrix}<\boldsymbol{0}\\ \begin{bmatrix}-\boldsymbol{Z} & *\\ \Phi_3(\boldsymbol{X},\boldsymbol{W}) & -\boldsymbol{X}\end{bmatrix}<\boldsymbol{0}\\ \sqrt{\mathrm{trace}(\boldsymbol{Z})}<\gamma_2\end{cases}\tag{45}$$

where trace($\boldsymbol{Z}$) is the trace of matrix $\boldsymbol{Z}$ and there are:

$$\begin{cases}\Psi_1(\boldsymbol{X},\boldsymbol{W})=(\boldsymbol{A}\boldsymbol{X}+\boldsymbol{B}_1\boldsymbol{W})+(\boldsymbol{A}\boldsymbol{X}+\boldsymbol{B}_1\boldsymbol{W})^{\mathrm{T}}+\alpha\boldsymbol{H}_{\mathrm{c}}\boldsymbol{H}_{\mathrm{c}}^{\mathrm{T}}\\ \Psi_2(\boldsymbol{X},\boldsymbol{W})=\boldsymbol{C}_\infty\boldsymbol{X}+\boldsymbol{D}_{\infty1}\boldsymbol{W}\\ \Psi_3(\boldsymbol{X},\boldsymbol{W})=\boldsymbol{E}_{\mathrm{a}}\boldsymbol{X}+\boldsymbol{E}_{\mathrm{b}}\boldsymbol{W}\\ \Phi_1(\boldsymbol{X},\boldsymbol{W})=(\boldsymbol{A}\boldsymbol{X}+\boldsymbol{B}_1\boldsymbol{W})+(\boldsymbol{A}\boldsymbol{X}+\boldsymbol{B}_1\boldsymbol{W})^{\mathrm{T}}+\beta\boldsymbol{H}_{\mathrm{c}}\boldsymbol{H}_{\mathrm{c}}^{\mathrm{T}}\\ \Phi_2(\boldsymbol{X},\boldsymbol{W})=\boldsymbol{E}_{\mathrm{a}}\boldsymbol{X}+\boldsymbol{E}_{\mathrm{b}}\boldsymbol{W}\\ \Phi_3(\boldsymbol{X},\boldsymbol{W})=(\boldsymbol{C}_2\boldsymbol{X}+\boldsymbol{D}_{21}\boldsymbol{W})^{\mathrm{T}}\end{cases}\tag{46}$$

In summary, the solution for the key matrix $\boldsymbol{P}$ in the sliding mode surface $\boldsymbol{S}$ can be obtained by (45). It should be noted that under the action of sliding mode control, the entire closed-loop system is mixed $\mathcal{H}_2/\mathcal{H}_\infty$ robustly stable. According to (21) and (22), the introduction of the control term v is for the design of the matrix $\boldsymbol{P}$, and thus the state feedback shown in (26) is entirely virtual, serving to construct the mixed $\mathcal{H}_2/\mathcal{H}_\infty$ robustly stable sliding mode surface matrix $\boldsymbol{P}$. At the same time, since no non-singular state transformation is required in the entire design, the design of the SMC is simplified.

C. Nonlinear Robust Sliding Mode Control of Excitation System

Combining the design of the SMC in Section III.A, the matrix $\boldsymbol{P}$ designed based on the mixed $\mathcal{H}_2/\mathcal{H}_\infty$ robust LMI in Section III.B, and the virtual control input

$\boldsymbol{u}=(\omega_0/H)(\dot{P}_e)$, the state feedback ONRSMC for the OMIBS that satisfies mixed $\mathcal{H}_2/\mathcal{H}_\infty$ robust performance can be obtained as:

$$V_f=\frac{x'_{d\Sigma}T_{d0}}{V_s\sin\delta}\left\{\begin{array}{l}\dfrac{H}{\omega_0}\boldsymbol{u}_{eq}+\dfrac{H}{\omega_0}\boldsymbol{u}_n-\\ V_s^2\left(\dfrac{x'_d-x_q}{x'_{d\Sigma}x_{q\Sigma}}\right)\Delta\omega\cos 2\delta\end{array}\right\}- \frac{T_{d0}E'_q\cos\delta}{\sin\delta}\Delta\omega+\frac{T_{d0}}{T'_d}E'_q-\frac{x'_d-x_q}{x'_{d\Sigma}}V_s\cos\delta \tag{47}$$

In addition, the saturation function sat(·) is used in the robust control term $\boldsymbol{u}_n$ instead of the sign function sgn(·) to reduce or eliminate chattering in the SMC. The saturation function is designed as:

$$\mathrm{sat}(\boldsymbol{S},\epsilon_c)=\begin{cases}1, & \boldsymbol{S}>\epsilon_c\\ \boldsymbol{S}/\epsilon_c, & |\boldsymbol{S}|\leqslant\epsilon_c\\ -1, & \boldsymbol{S}<-\epsilon_c\end{cases} \tag{48}$$

where ϵ_c is the saturation function coefficient.

The structure of the ONRSMC for the system based on feedback linearization is shown in Fig. 2.

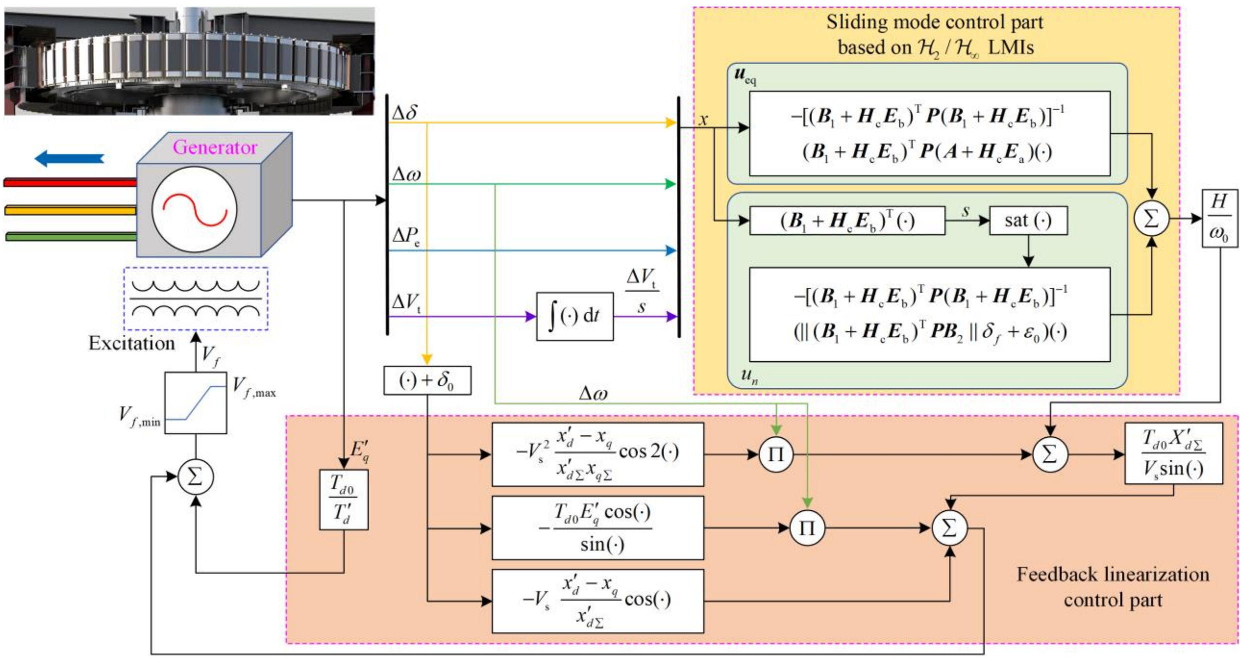

Fig. 2. Overall ONRSMC structure for excitation system.

IV. Adapative Salp Swarm Algorithm Based on Chaotic Map and its Application

A. Salp Swarm Algorithm

As shown in Fig. 3(a), the salps possess a transparent barrel-shaped body. They rely on contraction for movement and use their gelatinous body to pump water to complete the feeding process. One of their most intriguing behaviors is their tendency to live in groups. In deep-sea environments, salps often form tightly-knit aggregations called a salp chain, which is as illustrated in Figs. 3(b) and 3(c). A salp chain maintains close contact during swimming and foraging, with each individual continuously growing. However, the primary driving factors behind this unique behavior still need to be determined. Inspired by their observations of individual and group behaviors of salps in the ocean, Mirjalili developed a group intelligence-based optimization algorithm called the salp swarm algorithm (SSA) [57].

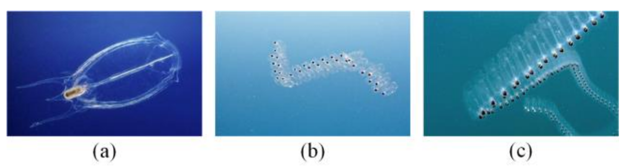

Fig. 3. Shape and structure of salp swarm in deep ocean. (a) Single salp. (b) Single salp chain. (c) Double salp chains.

The salp swarm is divided into two subpopulations: leaders and followers, with the leaders located at the front of the salp chain and the rest of the individuals as followers. The specific mathematical description of the salp swarm algorithm is as follows.

In the SSA, the salps predation space is assumed to be $N\times D$ dimensions. Then, the mathematical description of the population initialization is shown below:

$$X_{N\times D}=\mathrm{rand}(N,D)\times(ub-lb)+lb \tag{49}$$

where N is the population size; D is the dimension of space; "ub" and "lb" represent the upper and lower limits of the predation space, respectively, and the population initialization process is completely random.

Finding the optimal food source in the predation space is the goal of the population. In the population exploration phase, the location of the food source, which is the global optimal solution, influences the leader's position movement, and the leader's position is updated as follows:

$$x_j^i = \begin{cases} F_j + c_1[(ub_j - lb_j)c_2 + lb_j]c_3 \geqslant 0.5 \\ F_j - c_1[(ub_j - \mathrm{lb}_j)c_2 + lb_j]c_3 < 0.5 \end{cases} \tag{50}$$

where x_j^i represents the position of leader i in dimension j; F_j represents the position of the food source in dimension j; c_2 , c_3 are random numbers on [0,1]; and the mathematical description of parameter c_1 is shown below.

$$c_1 = 2\mathrm{e}^{-\left(\frac{4t}{T_{\max}}\right)^m} \tag{51}$$

where t and $T_{\max}$ represent the current iteration number and maximum iteration number, respectively; m is the power exponent of the constant. From (51), we can see that c_1 decreases nonlinearly with the increase of iterations. When the value of c_1 is larger, it is favorable to the exploration ability of the population, and vice versa, it is favorable to the local exploitation ability of the population, and the coefficient c_1 makes the exploitation and exploration ability of the population in a better balance.

In the SSA, the followers follow the leader and move in a way that satisfies Newton's second law. Thus, as shown in (52).

$$\begin{cases} x_j^i = at^2/2 + v_0\Delta t + x_j^i \\ a = (v_\mathrm{t} - v_0)/\Delta t \\ v_\mathrm{t} = (x_j^{i-1} - x_j^i)/\Delta t \end{cases} \tag{52}$$

where x_j^i represents the position of follower i in the jth dimension; x_j^{i-1} represents the position of follower $(i-1)$ in the jth dimension; a represents the acceleration; v_0 represents the initial velocity; and Δt is the difference of the number of iterations. Since the difference of the number of iterations $\Delta t = 1$ and the initial velocity $v_0 = 0$, (52) can be expressed as:

$$x_j^i = (x_j^i + x_j^{i-1})/2 \tag{53}$$

To further improve the solution accuracy and convergence speed of the SSA, while ensuring the algorithm achieves a balance between exploration and exploitation capabilities, this paper improves the algorithm performance in three key aspects, including: 1) population initialization; 2) leader position update; and 3) follower position update, while keeping the population individuals unchanged. These improvements are targeted at improving the convergence speed, enhancing the global search capability, and optimizing the local search performance, respectively. The schematic diagram of the improved framework is shown in Fig. 4, and the specific improvement process is described below.

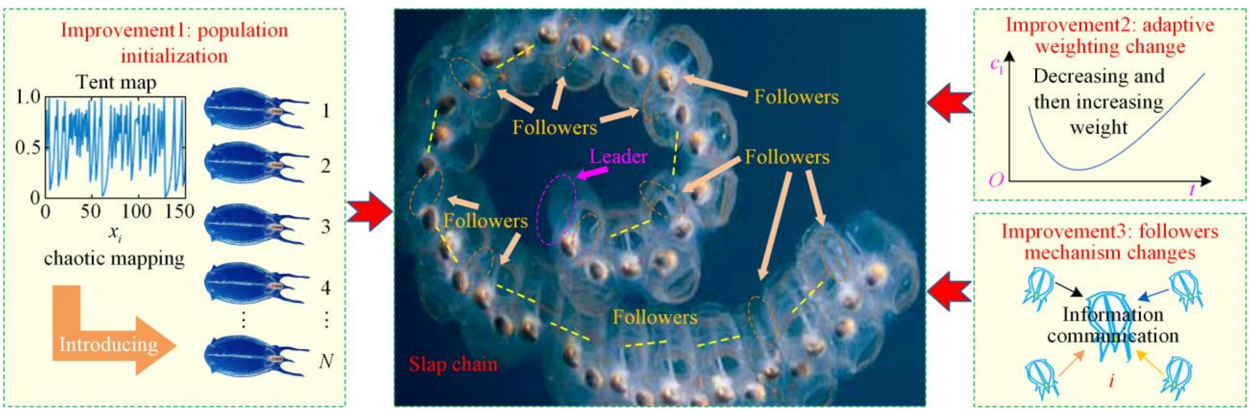

Fig. 4. Schematic diagram of the SSA improvement framework.

B. Three Improvements to SSA

As a key part of the population intelligence algorithm, the initialization position of population initialization directly affects the convergence speed and solution quality of the algorithm [58]. Compared with random distribution, uniform distribution has more comprehensive coverage in the solution space and is more likely to obtain good initial solutions. However, the basic SSA uses a random population initialization strategy, which cannot adequately cover the entire solution space. In contrast, chaotic sequences possess the characteristics of ergodicity, randomness, and regularity within a specific range [59]. Compared with random search, chaotic sequences can thoroughly probe the search space with higher probability, helping the algorithm to jump out of the local optimum and maintain the diversity of the population [60]. Table I shows the standard chaotic sequence functions, while their function value change curves are shown in Fig. 5 [17]. The symbolic values of chaotic functions in Table II are sourced from [18].

TABLE I
THE CHAOTIC MAPS FUNCTION

Chaotic-map	Function	Range
Gauss/mouse	$x_{k+1}=\begin{cases}1, y_k=0\\ \dfrac{1}{\mathrm{mod}(x_k,1)}, \text{otherwise}\end{cases}$	[−1,1]
Circle	$x_{k+1}=\mathrm{mod}(x_k+C_\mathrm{g}-C_\mathrm{e}\sin(2\pi x_k)/,1)$	[0,1]
Chebyshev	$x_{k+1}=\cos(k\cos^{-1}(x_k))$	[0,1]
Iterative	$x_{k+1}=\sin(C_\mathrm{I}\pi/x_k)$	[0,1]
Logistic	$x_{k+1}=C_\mathrm{L}x_k(1-x_k)$	[0,1]
Piecewise	$x_{k+1}=\begin{cases}C_\mathrm{P}^{-1}x_k, [0,C_\mathrm{P})\\ 10(x_k-C_\mathrm{P}), [C_\mathrm{P},0.5)\\ 10(1-C_\mathrm{P}-x_k), [0.5,1-C_\mathrm{P})\\ C_\mathrm{P}^{-1}(1-x_k), [1-C_\mathrm{P},1)\end{cases}$	[0,1]
Sine	$x_{k+1}=\sin(\pi x_k)$	[0,1]
Singer	$x_{k+1}=(C_\mathrm{S1}x_k+C_\mathrm{S2}x_k^2+C_\mathrm{S3}x_k^3+C_\mathrm{S4}x_k^4)$	[0,1]
Sinusoidal	$x_{k+1}=C_\mathrm{S5}x_k^2\sin(\pi x_k)$	[0,1]
Tent	$x_{k+1}=\begin{cases}C_\mathrm{T}^{-1}x_k, x_k<C_\mathrm{T}\\ C_\mathrm{T}^{-1}(1-x_k), x_k\geqslant C_\mathrm{T}\end{cases}$	[0,1]

TABLE II
SYMBOLIC VALUES OF CHAOTIC FUNCTIONS

Symbol	Value	Symbol	Value
C_g	0.2	C_S1	7.86
C_e	0.2/2π	C_S2	−23.31
C_I	0.7	C_S3	28.75
C_L	4	C_S4	−13.30
C_P	4	C_S5	2.3
		C_T	0.5

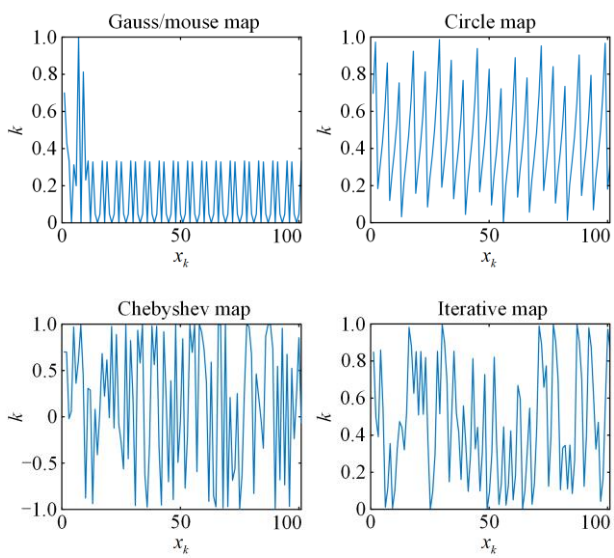

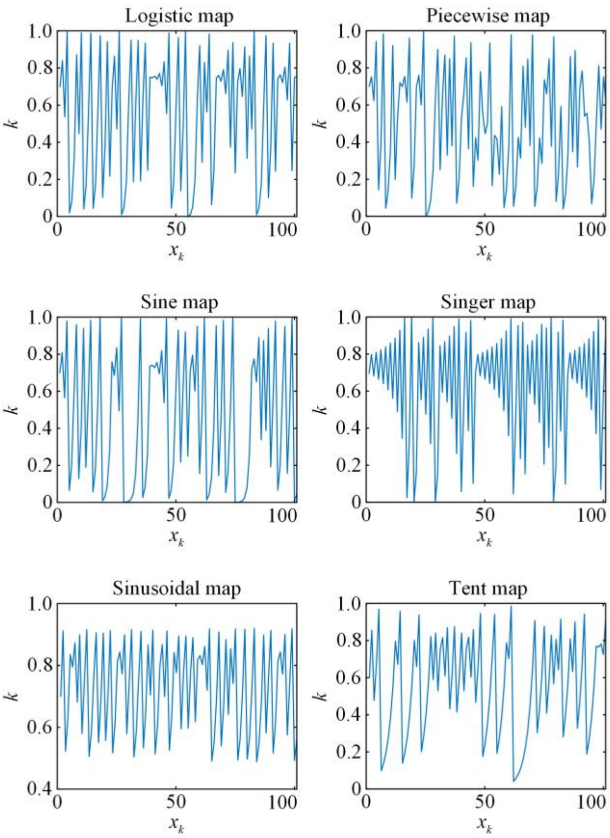

Fig. 5. Chaotic mapping image curve.

Therefore, in order to obtain a good initial solution position with a higher chance, the convergence speed of the population is accelerated. As can be seen in Fig. 5, the tent chaos mapping method has better traversal uniformity and faster iteration, so it is adopted in this paper to improve the coverage space of the initial solution. In the improved SSA, the tent chaos mapping is used to calculate the position of the initial solution in the algorithm, and its computational mathematical expression is:

$$y_{k+1}^i=\begin{cases}2x_k^i, & x_k^i<0.5\\ 2(1-x_k^i), & \text{else}\end{cases} \tag{54}$$

The inverse mapping yields the initial position of the population calculated as:

$$x_j^i=y_k^i(ub-lb)+lb \tag{55}$$

In summary, the chaotic mapping method described in (48) can substantially increase the coverage of the initial solution space, allowing the population to approach the optimal solution faster, and thus speed up the convergence of the algorithm.

Observation of (50) shows that the leader's position update in the population is mainly influenced by the food source and c_1. The larger the value of c_1, the better the exploration ability of the algorithm, whereas the smaller the value of c_1, the better the development ability of the algorithm. At the same time, the leader's position movement is also affected by the scaling factor c_2, which is a uniformly distributed random number and makes the leader's movement very blind, so the value of c_2 is mostly invalid.

The strategy of adding adaptive weights at the locations of the food sources helps to improve the performance of the optimization algorithm [61]. In the initial stage of the algorithm, the weights are large in order to provide the algorithm with sufficient exploration capability to help search the entire solution space. As the number of iterations increases, the weights gradually decrease, which helps enhance the ability of the algorithm to exploit the local range and allow the algorithm to better explore the local optimal solutions. However, in the middle and later stages of the algorithm, the weights start to gradually increase to give the leader the ability to jump out of the local optimal solution and avoid getting stuck in the local optimum. With this strategy, the algorithm is able to find the optimal solution more efficiently in the global context. The specific mathematical description of the improvement of (42) is shown as follows:

$$x_j^i = \begin{cases} F_j + c_1 F_j\,, & c_1 \geqslant 0.8 \\ F_j - c_1 F\,, & c_1 < 0.8 \end{cases} \tag{56}$$

$$c_1 = \begin{cases} 2\mathrm{e}^{-\left(\frac{2t}{T_{\max}}\right)}, & t < T_{\max}/2 \\ 2\mathrm{e}^{-\left[2\frac{(T_{\max}-t)}{T_{\max}}\right]}, & t \geqslant T_{\max}/2 \end{cases} \tag{57}$$

where F_j is the food source position and c_1 is the decreasing and then increasing weight.

In the basic SSA algorithm, the movement of the followers can be described as (53). From (53), it can be seen that the position movement of the ith individual is only influenced by the $(i-1)$th individual without considering the adaptation of the previous individual. Therefore, the position movement of the follower is somewhat blind, i.e., the position movement of each follower i is only related to individual $(i-1)$ and lacks the ability to exchange information with other individuals. This kind of movement may lead the algorithm into a local optimum. To overcome the drawbacks, an improved follower movement approach is proposed, which is mathematically described as:

$$x_j^i = \begin{cases} (x_j^\eta + F_\mathrm{a} x_j^i)/2\,, & f(x_j^\eta) \leqslant f(x_j^i) \\ x_j^i - \sin(x_j^i)\,, & f(x_j^\eta) > f(x_j^i) \end{cases} \tag{58}$$

where F_a is a decreasing weight factor with the number of iterations and η represents the individual randomly selected from the leader.

If the adaptation of the current individual i is greater than the adaptation of the leader η, the weight factor is added to the position of the individual with greater adaptation to reduce the influence of the individual in the worse position and improve the weight of the better individual. Otherwise, the individual i only fluctuates around itself. This method of movement can greatly reduce the blind following and enhance the information exchange between populations, while preserving the information of followers themselves and ensuring the diversity of populations.

By adding chaotic mapping and adaptive weights and changing the position update of leaders and followers at the same time, an adaptive salp swarm algorithm based on chaotic mapping (CASSA) is obtained. CASSA balances the exploration and exploitation abilities of leaders, reduces follower blindness, and better preserves individual information while ensuring the diversity of the population. The specific algorithm flow of CASSA is shown in Fig. 6.

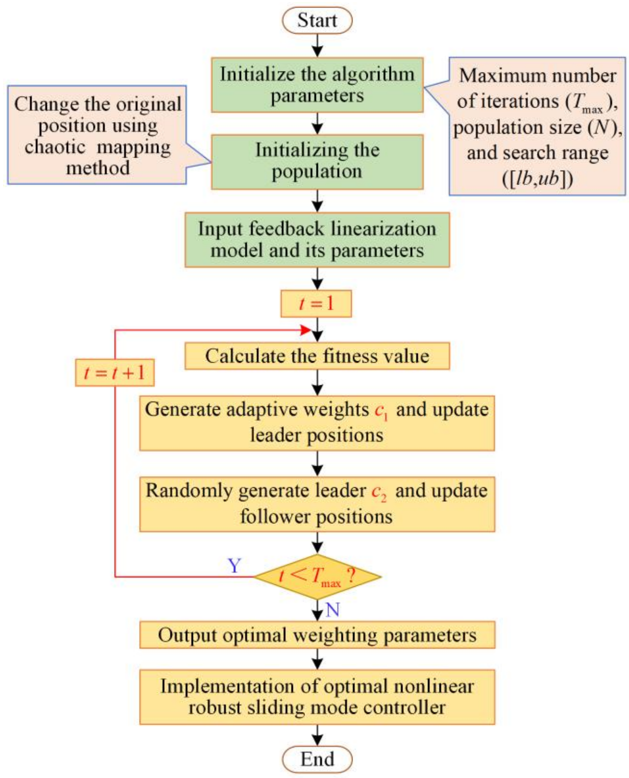

Fig. 6. The specific algorithm flow of CASSA.

C. Applying CASSA Algorithm to ONRSMC of the OMIBS

In the definition of the hybrid robust performance output vector weights described in the previous section, it is noted that the selection of the parameters $q_{ij}, r_i > 0\ (i = 1,2; j = 1,2,3,4)$ in the weight matrices $\boldsymbol{Q}_\infty$, $\boldsymbol{Q}_2$, $\boldsymbol{R}_\infty$ and $\boldsymbol{R}_2$ in the performance output vector is crucial, as they determine whether the system can achieve the expected performance metrics. Also, the choice of ε_0 and ϵ_c in ONRSMC impacts the control performance output. In previous studies, the selection of these controller parameters usually relies on the designer's experience, which often fails to exploit fully the optimal performance of the controller.

To solve this problem, a two-stage optimization of ONRSMC is proposed here. The specific optimization framework is schematically shown in Fig. 7. As shown, the optimization for the parameters in ONRSMC is divided into two stages. In stage I, the number of parameters is appropriately adjusted to 10 by the CASSA algorithm to fully optimize the weight parameters q_{ij} and r_i (where $i=1,2;\ j=1,2,3,4$), so that the robust performance of ONRSMC can be optimized. In stage II, the switching gain ε_0 of the sliding mode control part of ONRSMC and the coefficient ϵ_c of the saturation function $\text{sat}(\cdot)$ are adjusted by the CASSA algorithm to make the sliding mode performance of ONRSMC optimized. In both optimization processes, the system faults considered are generator outlet short-circuit faults. The system optimization objective function is defined as:

$$O_{\text{bj}} = \int (\Delta\omega^2 + \Delta V_t^2)\mathrm{d}t \tag{59}$$

where O_{bj} denotes the value of the objective function throughout the optimization process; ΔV_t denotes the deviation of the generator outlet voltage; and $\Delta\omega$ indicates the generator speed deviation.

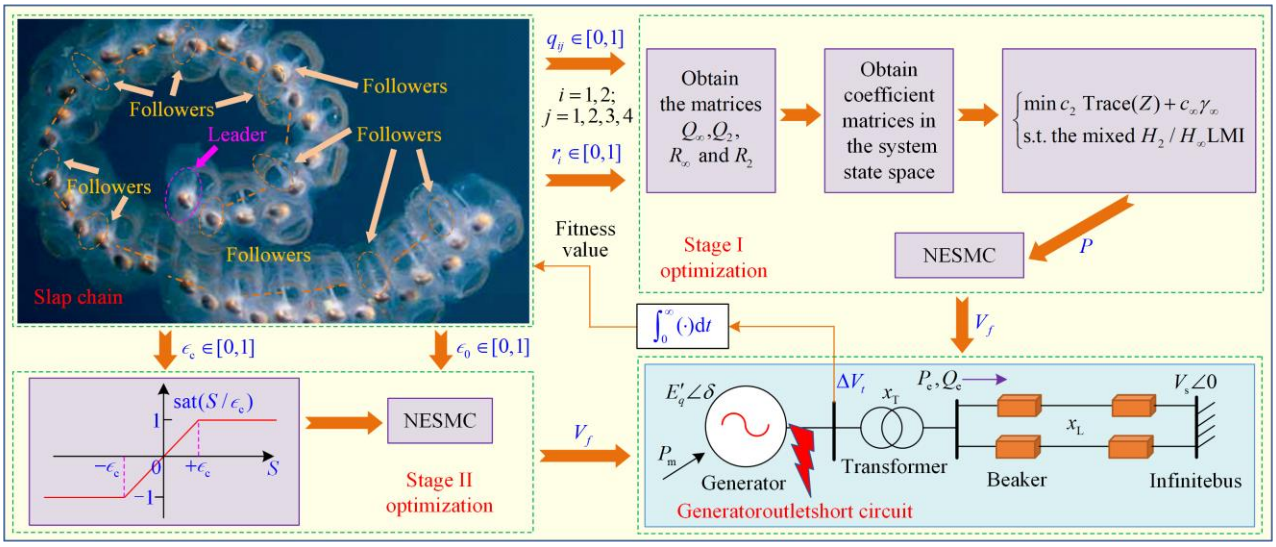

Fig. 7. Schematic diagram of the proposed two-stage optimization framework.

V. Numerical Study

Control process simulations are conducted in a single-machine infinite-bus system to verify the effectiveness of the proposed controller applied to the excitation system. As shown in Fig. 8, there are three simulation cases. By comparing the proposed excitation control method with the conventional methods commonly used in engineering applications, the superior control performance of the proposed method is demonstrated. Specifically, to validate the effectiveness of the proposed controller in the excitation system, this section compares the performance of this controller with traditional PID control, PID+PSS, and a nonlinear robust controller (NRC) on the power system shown in Fig. 1. The transfer function of the PID controller is given as:

$$V_f = K_{\text{p}}\Delta V_t + K_i\int \Delta V_t \mathrm{d}t + \frac{\mathrm{d}}{\mathrm{d}t}\Delta V_t \tag{60}$$

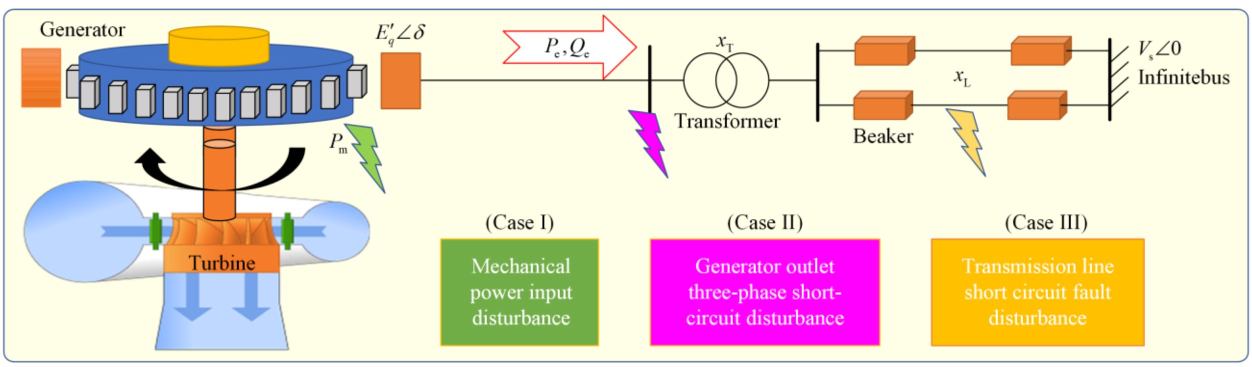

Fig. 8. Three simulation cases.

The mathematical model of the PSS is shown in Fig. 9 [62]. The design of the NRC is based on the method proposed in [63], and its mathematical expression is described as:

$$
\begin{aligned}
V_f = {} & \frac{x'_{d\Sigma}T_{d0}Hf_1}{\omega_0 V_s \sin\delta}\Delta\delta + \left(\frac{x'_{d\Sigma}T_{d0}Hf_2}{\omega_0 V_s \sin\delta} - \frac{T_{d0}E'_q\cos\delta}{\sin\delta}\right)\Delta\omega + \\
& \frac{x'_{d\Sigma}T_{d0}Hf_3}{\omega_0 V_s \sin\delta}\Delta P_e + \frac{x'_{d\Sigma}T_{d0}Hf_4}{\omega_0 V_s \sin\delta}\int \Delta V_t \mathrm{d}t + \\
& \frac{x'_{d\Sigma}T_{d0}}{V_s\sin\delta}\left(\frac{x'_d - x_q}{x'_{d\Sigma}x_{q\Sigma}}\right)V_s^2\Delta\omega\cos 2\delta + \\
& \frac{T_{d0}}{T'_d}E'_q - \frac{x'_d - x_q}{x'_{d\Sigma}}V_s\cos\delta
\end{aligned}
\tag{61}
$$

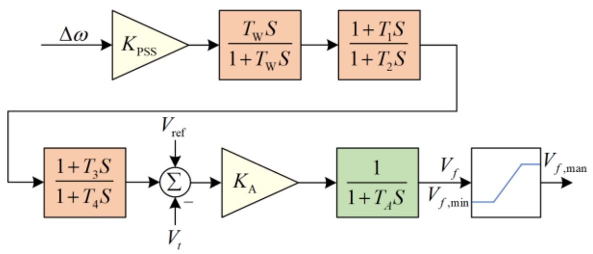

Fig. 9. Block diagram of the PSS excitation regulator.

A. Simulation Parameters

The structure of the OMIBS used in the study is shown in Fig. 1. In the infinite 230 kV system, the parameters of the power system components are: $H = 12.9$ s, $D = 0.075$, $x_d = 1.652$, $x'_d = 0.209$, $x_q = 1.0738$, $T_{d0} = 6.55$ s, $x_T = 0.0584$, and $x_L = 0.0532$. The initial steady-state operating conditions of the system are: $P_{e0} = 0.706$, $\delta_0 = 42.6^\circ$, $\omega_0 = 314.16$ rad/s, $E'_{q0} = 0.936$, and $V_{t0} = 1.05$.

The parameters for the PID controller are: $K_p = 100$, $K_i = 50$, and $K_d = 10$. The parameters used for the PSS are shown in Table III, while the feedback matrix of the NRC is also designed based on the optimal mixed LMIs, with the specific expression of the feedback matrix being $f_1 = 139$, $f_2 = 64$, $f_3 = -266$, and $f_4 = -634$. To ensure the stable operation of the generator, the excitation voltage satisfies the constraint condition of $|V_f| \leqslant 10$ p.u.

TABLE III
PSS EXCITATION REGULATOR PARAMETERS

Parameters	Value	Parameters	Value (s)
K_{PSS}	15	T_1	0.3
K_A	40	T_2	0.5
T_A	0.005 s	T_3	0.3
T_W	5 s	T_4	0.5

For the proposed controller in this paper, $|\Delta D|$ is defined as $0.1D$, $|\Delta H| = 0.1H$, $|\Delta R_V| = 0.1R_V$, and $|\Delta S_V| = 0.1S_V$ in (15). Therefore, the calculated results of the coefficient matrices of the mathematical model containing uncertainties are as follows:

$$
\begin{cases}
\boldsymbol{A} = \begin{bmatrix} 0 & 1 & 0 & 0 \\ 0 & -0.058 & -24.3 & 0 \\ 0 & 0 & 0 & 0 \\ -0.171 & 0 & 0.129 & 0 \end{bmatrix} \\
\boldsymbol{B}_1 = [0 \quad 0 \quad 0.0412 \quad 0]^{\mathrm{T}} \\
\Delta\boldsymbol{B}_1 = [0 \quad 0 \quad -0.00412 \quad 0]^{\mathrm{T}} \\
\boldsymbol{B}_2 = [0 \quad 24.3 \quad 0.412 \quad 0.129]^{\mathrm{T}} \\
\Delta\boldsymbol{A} = \begin{bmatrix} 0 & 0 & 0 & 0 \\ 0 & -0.0058 & -24.3 & 0 \\ 0 & 0 & 0 & 0 \\ -0.038 & 0 & 0.0144 & 0 \end{bmatrix}
\end{cases}
\tag{62}
$$

In (17), the matrices $\boldsymbol{H}_c$, $\boldsymbol{E}_a$, and $\boldsymbol{E}_b$ are taken as:

$$
\begin{cases}
\boldsymbol{H}_c = \begin{bmatrix} 0.2 & 0 & 0 & 0 \\ 0 & 0.2 & 0 & 0 \\ 0 & 0 & 0.2 & 0 \\ 0 & 0 & 0 & 0.2 \end{bmatrix} \\
\boldsymbol{E}_a = \begin{bmatrix} 0 & 0 & 0 & 0 \\ 0 & -0.0064 & -13.5 & 0 \\ 0 & 0 & 0 & 0 \\ -0.19 & 0 & 0.0714 & 0 \end{bmatrix} \\
\boldsymbol{E}_b = [0 \quad 0 \quad -0.0206 \quad 0]^{\mathrm{T}}
\end{cases}
\tag{63}
$$

The weighting coefficients q_{ij} and r_i in (30) are optimized using the aforementioned CASSA. The optimization framework is shown in the stage I of Fig. 7, while the iteration curve of the optimization process is shown in Fig. 10. It can be seen from Fig. 10 that CASSA can avoid local optima and requires a smaller number of iterations in the optimization process. After completing the optimization in the first stage, the switching coefficient ε_0 and the saturation function coefficient ϵ_c in the proposed controller are optimized. The iteration curve of the second stage optimization process is shown in Fig. 11, and the optimization results are shown in Table IV.

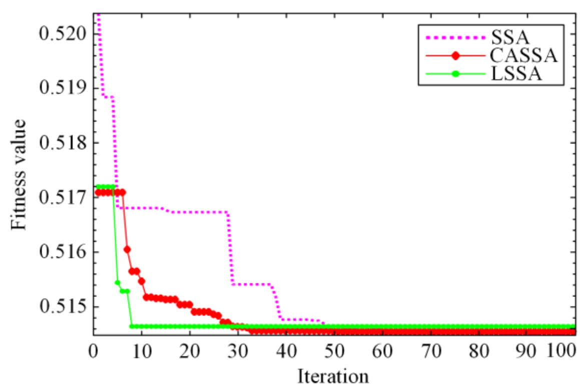

Fig. 10. Iteration curve for stage I of the optimization process.

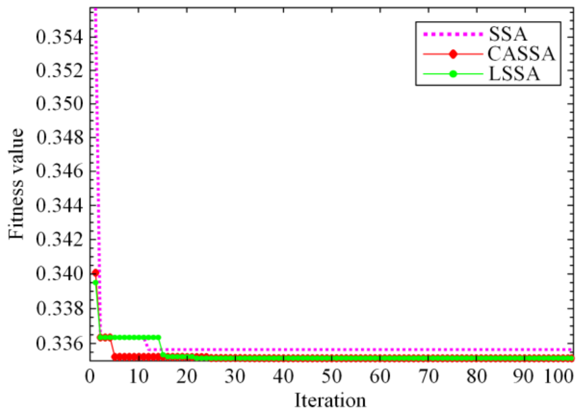

Fig. 11. Iteration curve for stage II of the optimization process.

TABLE IV
OPTIMIZATION RESULTS OF THE PROPOSED METHOD

Proposed method	Optimization results	Proposed method	Optimization results
q_{11}	31.4485	q_{13}	0
q_{12}	3.6000	q_{14}	7.5597
q_{13}	0	r_1	0.0118
q_{14}	7.3632	r_2	0.0079
q_{21}	3.1299	ε_0	1
q_{12}	1.6322	ϵ_c	0.0202

From Figs. 10 and 11, significant improvements brought by the two-stage optimization process can be clearly observed. With the proposed controller, the fitness value of the excitation system has been successfully reduced from the initial 0.517 to 0.33, demonstrating the achievement of the optimization process. In addition, by comparing Figs. 10 and 11, an important finding is that, for the controller proposed in this study, optimizing only the weights in the performance output vector is not sufficient to fully unleash its potential performance. Therefore, combining the optimization processes in the two stages will be more helpful in achieving the optimal performance of the controller. The achievements made in this study provide a reference for subsequent relevant SMC optimization designs.

B. Case I

In this study, we conduct a simulation analysis of the proposed controller to verify its dynamic response characteristics. In this case, the mechanical power P_m undergoes a step increase of 0.2 p.u. at 30 s, and then swiftly returns to its rated value at 30.2 s. The dynamic response characteristics of various controllers are depicted in Fig. 12. It is evident from Fig. 12 that the proposed controller can suppress oscillations induced by the step increase in the shortest time, demonstrating its superior dynamic response. Concurrently, under the influence of the proposed controller, the oscillations caused by faults are significantly suppressed, validating the high efficiency of the controller in handling system faults. Also, by adopting a saturation function, the chattering phenomenon present in the sliding mode control is successfully mitigated, resulting in a smoother control input. This not only contributes to enhancing the stability of the system but also helps reduce equipment wear and prolong its lifespan.

It is worth noting that although the terminal voltage V_t of the proposed controller exhibits a smaller oscillation amplitude than other controllers, it possesses a faster convergence speed. This suggests that the controller has a higher response rate in dealing with voltage fluctuations, ensuring system stability when facing transient events.

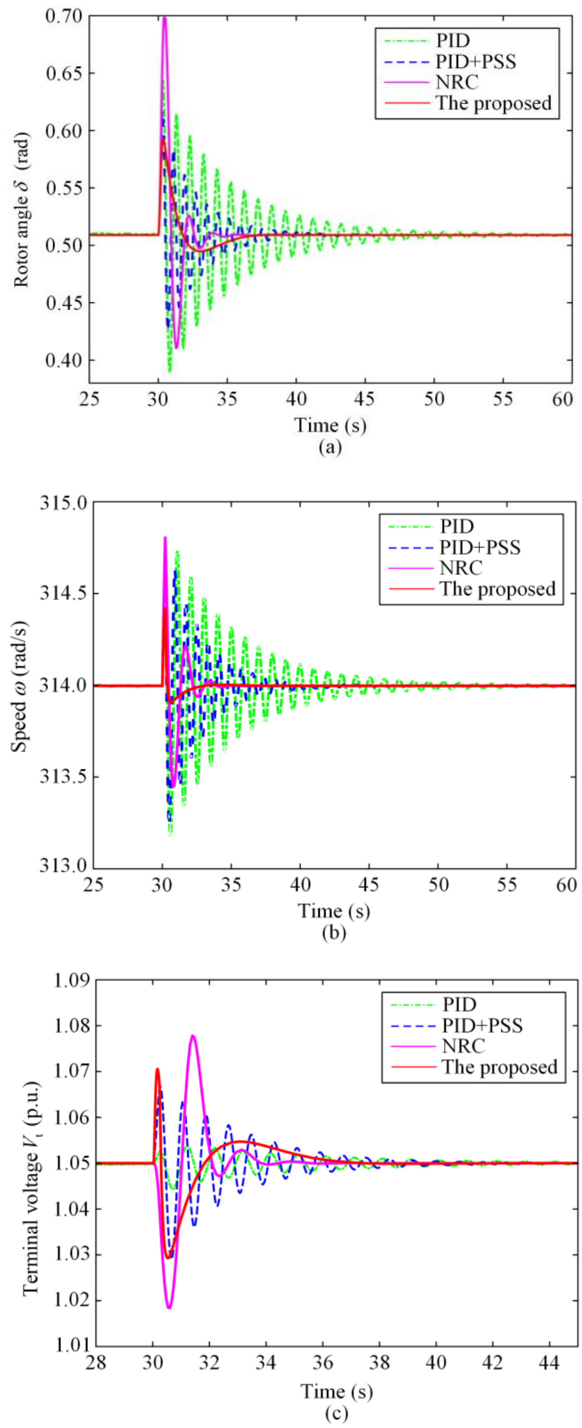

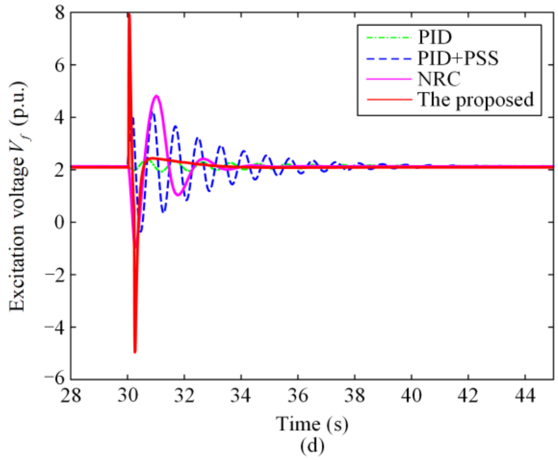

Fig. 12. System responses obtained in Case I. (a) Rotor angle. (b) Speed. (c) Terminal voltage. (d) Excitation voltage.

C. Case II

Figure 13(a) illustrates the variations of the system rotor angle during a three-phase fault at the generator's output. It is evident from Fig. 13(a) that among all the controllers, the proposed controller exhibits the fastest control speed with the smallest overshoot. Figure 13(b) shows the variations of the system's speed. As can be seen, PID, PSS, and NRC all produce a certain degree of oscillations. Also, the excitation system exhibits significant oscillations with PID and PSS. However, the proposed controller has the smallest overshoot.

Figures 13(c) and (d) illustrate the variations of the system's terminal and excitation voltages, respectively, during a three-phase fault at the generator's output. It can be seen that PID, PSS, NRC, and the proposed controller can all effectively control the terminal voltage. As for the excitation voltage variations shown in Fig. 13(d), the proposed controller exhibits the smallest overshoot of all controllers, indicating that it can achieve system stability at a lower control cost. In contrast, the excitation voltage with the other three controllers exhibits significant oscillations.

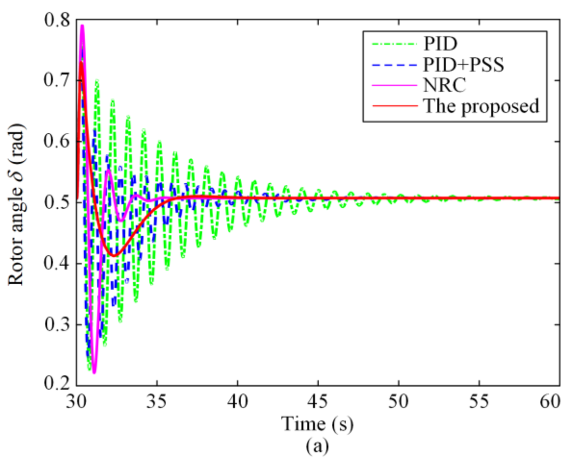

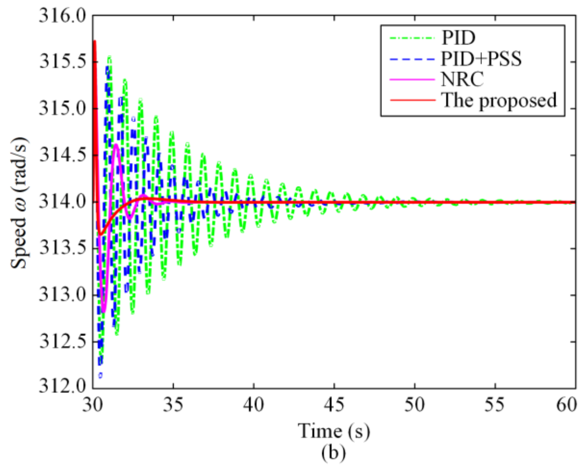

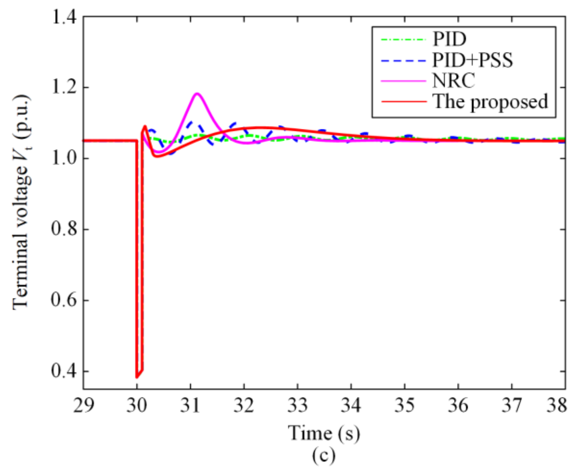

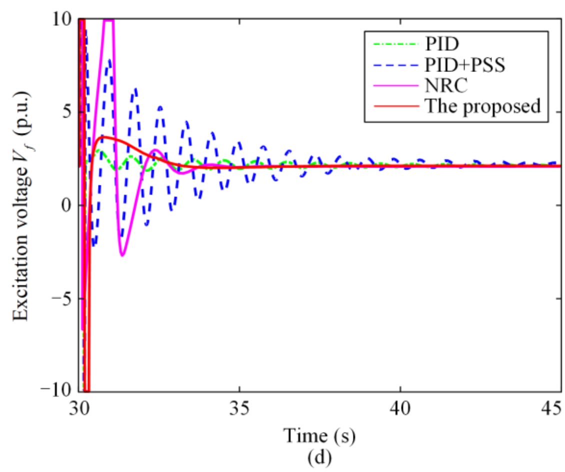

Fig. 13. System responses obtained under Case II. (a) Rotor angle. (b) Speed. (c) Terminal voltage. (d) Excitation voltage.

D. Case III

When a short-circuit fault occurs in the power system, the current in the power grid will suddenly become very large, which may cause oscillations in the power system and affect its stability and reliability. Thus, an effective controller is usually needed to control the operation of the power system to ensure that normal operation can be restored as quickly as possible in the event of a fault.

To verify the effectiveness of the proposed controller in system fault conditions, a system fault is applied in Case III as follows: a three-phase short circuit occurs in the transmission line, the line trips at $t=30$ s, and the automatic reclosing device starts at $t=30.1$ s. The simulation results are shown in Fig. 14. It shows that the proposed controller can effectively damp power system oscillations caused by the fault in the shortest possible time. Shortly after the occurrence of the short-circuit fault, the automatic reclosing device starts, and the proposed controller can quickly and effectively adjust the power system to ensure that it can return to normal operation.

In summary, the proposed controller has good robustness and adaptability, can adapt to different types of power system faults, and can ensure the stability and reliability of the power system in a variety of conditions. These results indicate that the proposed controller has good performance and application prospects, and can improve the stability and reliability of the power system.

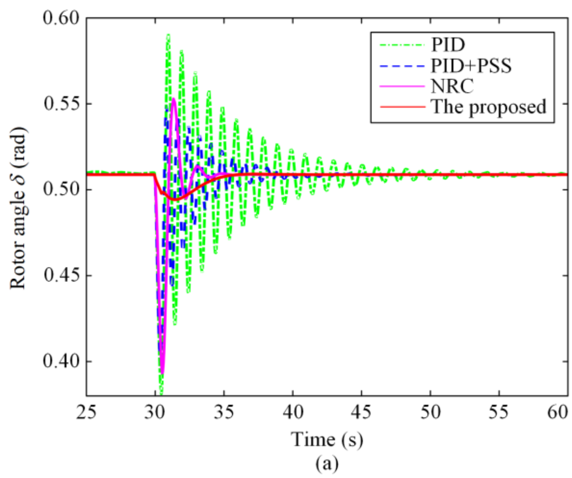

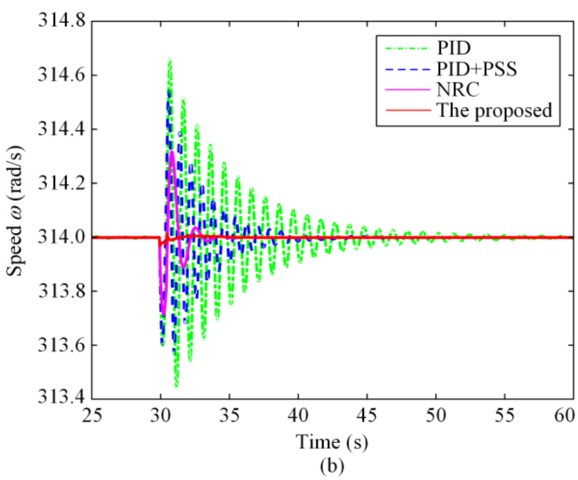

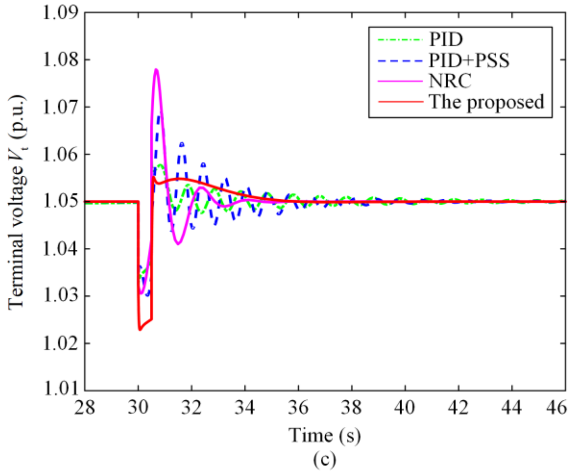

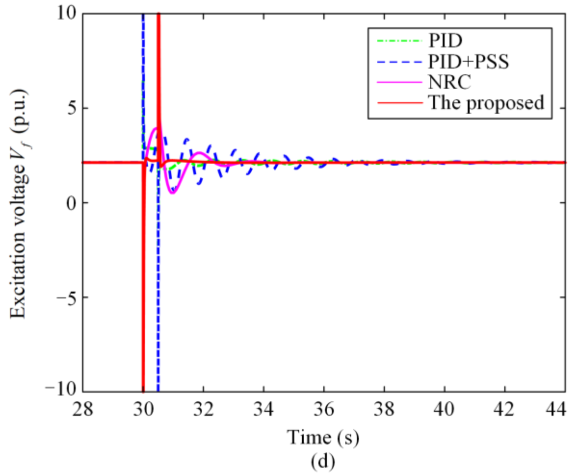

Fig. 14. System responses obtained in Case III. (a) Rotor angle. (b) Speed. (c) Terminal voltage. (d) Excitation voltage.

E. Robustness Against System Parameters' Change

In this subsection, a comprehensive analysis of the robustness of controllers is conducted with the uncertainty of generator parameters. To evaluate the performance, studies are carried out when the *d*-axis impedance (x_d) and *d*-axis transient time constant (T_{d0}) experience a 50% measurement error around their nominal values. Such parameter variations may lead to significant shift in the system operating state, thus affecting the performance of the controllers.

Figure 15 illustrates the system response curves during a short-circuit fault, as presented in Case III, when both parameters are subjected to a 50% measurement error. It is evident that the performance of PID and PSS controllers notably lags behind the other two robust controllers as the operating point shifts. This is mainly attributed to the fact that PID and PSS controllers have higher demand for the accuracy of system parameters, and thus their control performance is significantly impacted when parameter uncertainties arise.

In addition, although the NRC controller exhibits outstanding performance under accurate system models, its control performance is inevitably affected in the event of measurement errors. This is because of the NRC controller's reliance on precise system models, and so once errors occur in the model, its control performance is compromised. In comparison to other controllers, the proposed controller possesses enhanced robustness. This can be primarily credited to its approach to handling parameter uncertainties, which allows it to maintain consistent control performance even when confronted with such uncertainties.

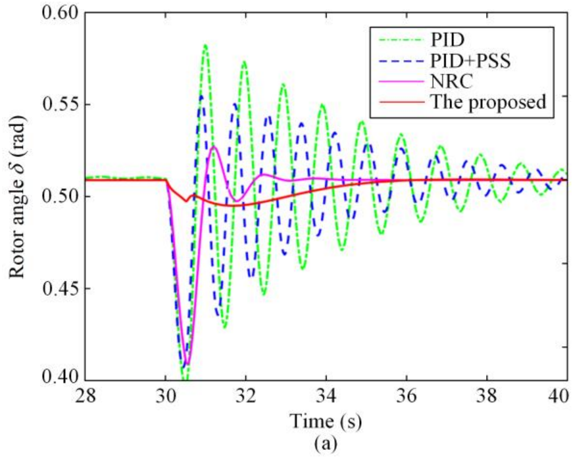

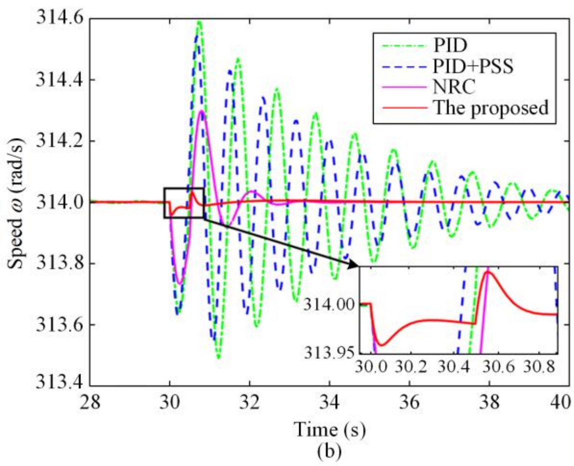

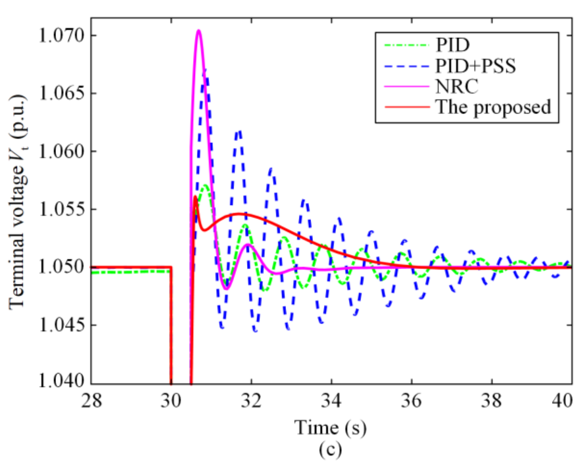

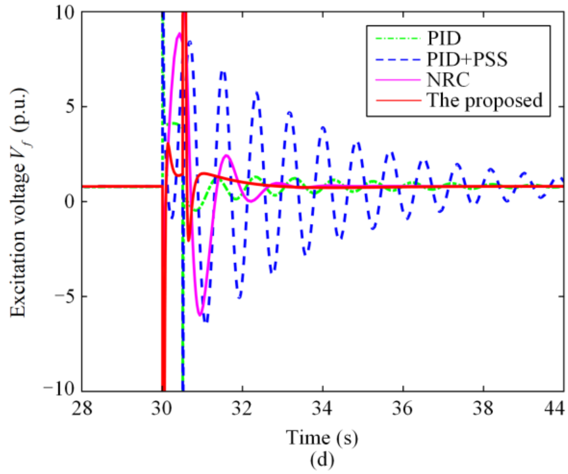

Fig. 15. System responses obtained with a short-circuit fault with parameter uncertainties. (a) Rotor angle. (b) Speed. (c) Terminal voltage. (d) Excitation voltage.

Further studies on the controller performance are conducted when T_{d0} and x_d experience ±50% measurement errors around their nominal values. By comparing the system responses in Figs. 16(a) and (b), it is found that the proposed controller can achieve minimal system speed variation with these two parameter uncertainties, thus proving the robustness of the controller.

To further verify the controller's performance under parameter uncertainty, cases where the unit's rotational inertia H and the time constant of the excitation winding T_{d0} experience ±50% perturbations within the nominal value range are investigated. In these conditions, the responses of the system's maximum speed are shown in Figs. 16(c) and 16(d). As seen, it is evident that the red lines remain flat, indicating that the maximum speed responses do not differ significantly with different parameter values with the proposed controller. This finding further confirms the proposed controller's ability to maintain good performance when there are parameter perturbations.

In summary, this study validates the proposed controller's robustness and control capabilities through uncertainty analysis of key parameters such as T_{d0} and x_d , unit rotational inertia, and the time constant of excitation windings. This implies that in practical applications, even in the presence of parameter measurement errors or system parameter perturbations, the proposed controller can still achieve stable and efficient generator control. The results provide strong support for improving the stability and reliability of power systems, while also offering a reference control scheme for subsequent research.

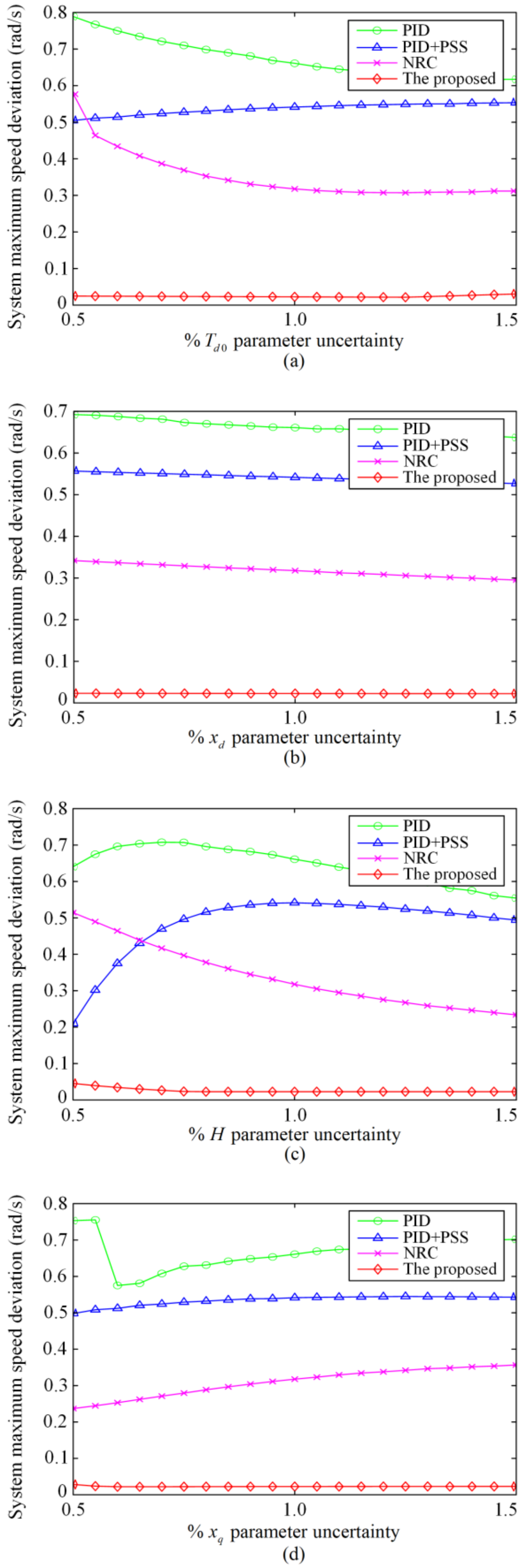

Fig. 16. System robustness with parameter uncertainties.

F. Comprehensive Performance Comparison

Performance comparison refers to the evaluation of the overall performance of different controllers by comparing their performance from multiple aspects. In this paper, the integral of absolute error (IAE) index is used to evaluate the tracking performance and robustness of the controllers. The IAE index of each controller in different scenarios is shown in Table V, and it is defined as:

$$IAE_x = \int_{t_a}^{t_b} \left| x - x^* \right| \mathrm{d}t \tag{64}$$

where x^* is the reference value of variable x; and the integration time from $t_b = 30$ s to $t_a = 50$ s represents a simulation dynamic process time of 20 s.

TABLE V
IAE INDICES OF DIFFERENT CONTROL SCHEMES CALCULATED IN DIFFERENT CASES

Simulation cases		Controllers			
		PID	PID+PSS	NRC	The proposed
I	IAE_δ	0.3072	0.1628	0.1758	0.1065
	IAE_ω	1.9971	1.2679	0.6451	0.1946
	IAE_{V_t}	0.0115	0.0329	0.0377	0.0327
	IAE_δ	0.7960	0.4755	0.3286	0.3594
II	IAE_ω	5.0444	3.3839	1.3123	0.6333
	IAE_{V_t}	0.1288	0.1626	0.1584	0.1804
	IAE_δ	0.2460	0.1329	0.0976	0.0432
III	IAE_ω	1.5188	0.9105	0.3544	0.0311
	IAE_{V_t}	0.0182	0.0307	0.0263	0.0266

As shown in Table V, by comparing the IAE indices of different controllers in different scenarios, it can be concluded that the proposed controller has the lowest IAE index in the majority of scenarios. Specifically, in Case I, the IAE_ω of the proposed controller is only 90.26% of PID control, 84.65% of PSS control, and 69.83% of NRC. This indicates that the proposed controller has better performance and robustness in tracking the reference signal, and has a smaller error level than other controllers.

Finally, the study investigates the control cost required by each controller in the three scenarios. In this paper, control cost is defined as:

$$J_{\text{cost}} = \int_{t_a}^{t_b} \left| V_f \right| \mathrm{d}t \tag{65}$$

The total control cost is obtained by integrating the excitation voltage V_f, which reflects the overall control output of each controller in each scenario. If the total control cost is low, it means that the required total control voltage is also low, indicating better controller performance.

Table VI shows the total control cost required by the four controllers in the three cases. It can be seen that the proposed controller requires a lower total control cost than the nonlinear NRC in all scenarios, indicating better performance of the proposed controller. However, in Case I with mechanical power step change and Case II with three-phase short circuit fault, the total control cost of the proposed controller is higher than those of PID. This is because the proposed controller uses higher control gain to recover the disturbed system more quickly, resulting in an increase in the total control cost.

TABLE VI
OVERALL CONTROL COSTS OF DIFFERENT CONTROLLERS REQUIRED IN DIFFERENT CASES

Cases	Controllers			
	PID	PID+PSS	NRC	The proposed
I	0.6118	4.2023	3.2455	1.9351
II	2.7745	11.9598	9.2953	5.7500
III	0.9541	3.0997	2.0585	0.8761

VI. CONCLUSION

This paper presents an optimal nonlinear robust sliding mode control strategy for excitation systems based on mixed $\mathcal{H}_2/\mathcal{H}_\infty$ LMIs. The developed method effectively addresses the challenges of parametric uncertainties, external disturbances, and nonlinearities in the excitation system, resulting in improved stability and performance of the overall power system. The proposed control scheme combines the strengths of SMC, $\mathcal{H}_2$, and $\mathcal{H}_\infty$ optimization techniques, and offers a robust and versatile solution that can be applied to a wide range of excitation systems. The incorporation of LMIs facilitates a systematic approach to controller synthesis, ensuring a tractable and computationally efficient design process. Additionally, CASSA is used for tuning the parameters of the proposed controller, ensuring that optimal performance is fully realized.

To validate the effectiveness of the proposed control strategy, numerical simulations are carried out, demonstrating significant improvements in transient response, system stability, and robustness against uncertainties and disturbances when compared to conventional control methods such as PID and PSS. The performance of the designed controller is found to be superior to existing nonlinear robust control techniques. In summary, the presented ONRSMC of the excitation system based on mixed $\mathcal{H}_2/\mathcal{H}_\infty$ LMIs provides a valuable reference for the development of advanced control techniques, which can ensure a stable, reliable, and efficient power system.

ACKNOWLEDGMENT

Not applicable.

AUTHORS' CONTRIBUTIONS

Yidong Zou: conceptualization, methodology, validation and writing original draft preparation. Yunhe Wang: validation and simulation. Jinbao Chen: supervision. Wenqing Hu: software and validation. Yang Zheng: simulation and writing-reviewing. Wenhao Sun: writing-reviewing and editing. Zhihuai Xiao: supervision. All authors read and approved the final manuscript.

FUNDING

This work is supported by the National Natural Science Foundation of China (No. 51979204 and No. 52009096), the Fundamental Research Funds for the Central Universities (No. 2042022kf1022), and the Hubei Provincial Natural Science Foundation of China (No. 2022CFD165).

AVAILABILITY OF DATA AND MATERIALS

Not applicable.

DECLARATIONS

The authors declare that they have no known competing financial interests or personal relationships that could have appeared to influence the work reported in this article.

AUTHORS' INFORMATION

Yidong Zou received the B.S. degree in energy power engineering from Hebei University of Engineering and the M.S. degree in energy power engineering from Kunming University of Technology in 2019 as well as 2022, respectively. Since September 2022, he has been a Ph.D. student in the Key Laboratory of Hydromechanical Transition Processes, Ministry of Education, Wuhan University. His research interests include fault diagnosis and optimal control of hydropower processes.

Yunhe Wang received her B.S. degree in energy and power engineering from Wuhan University in 2017 and her M.S. in thermal energy engineering in 2020. She is currently pursuing her Ph.D. in Fluid Machinery and Engineering at Wuhan University. Her current research interests include graph learning and deep learning in industrial applications, with an emphasis on the machine-learning-based fault diagnosis and remaining life prediction.

Jinbao Chen received the B.S. and M.S. degrees in energy power engineering from North China University of Water Resources and Hydropower in 2017 as well as 2020, respectively. Since September 2020, he has been a Ph.D. student in the Key Laboratory of Hydromechanical Transition Processes, Ministry of Education,

Wuhan University. His research interests include fault diagnosis and optimal control of hydropower processes.

Wenqing Hu received his B.S. and M.S. degrees in turbine engineering from Wuhan University of Technology in 2019 and 2022, respectively. Since September 2022, he has been a Ph.D. student in the Key Laboratory of Hydromechanical Transition Processes of the Ministry of Education, Wuhan University. His research interests include fault diagnosis and optimal control of hydropower processes and deep learning applications in power systems.

Yang Zheng received his B.E. degree in electrical engineering and automation from Huazhong University of Science and Technology (HUST) in 2013, and he received his Ph.D. in water resources and hydropower engineering from HUST in 2018. He is currently a distinguished associate researcher at the School of Power and Mechanics, Wuhan University. His research interests include modeling and control of hydropower/pumped storage units, principles and applications of hydraulic transient flow, and analysis and device design of ocean energy generation systems

Wenhao Sun received the B.S. degree in energy power engineering from North China University of Water Resources and Hydropower in 2021. From September 2021 to now, he has been a graduate student at Wuhan University. His research interests include data-driven fault diagnosis of hydropower units based on and optimal control of hydropower processes.

Zhihuai Xiao received the Ph.D. degree in water resources and hydropower engineering from the Huazhong University of Science and Technology, Wuhan, China, in 2004. He is currently a professor with the School of Power and Mechanical Engineering, Wuhan University, Wuhan. He has authored or coauthored more than 150 scientific papers in refereed journals, book chapters, and conference proceedings. His research interests include condition monitoring and fault diagnosis for hydraulic machineries, and modeling, simulation and optimal control for hydro-turbine regulating systems

REFERENCES

[1] S. Singh, S. Saini, and S. K. Gupta *et al*., "Solar-PV inverter for the overall stability of power systems with intelligent MPPT control of DC-link capacitor voltage," *Protection and Control of Modern Power Systems*, vol. 8, no. 1, pp. 1-20, Jan. 2023.

[2] F. Ahsan, N. H. Dana, and S. K. Sarker *et al*., "Data-driven next-generation smart grid towards sustainable energy evolution: techniques and technology review," *Protection and Control of Modern Power Systems*, vol. 8, no. 3, pp. 1-42, Jul. 2023.

[3] G. Cai, S. Zhou, and C. Liu *et al*., "Hierarchical under frequency load shedding scheme for inter-connected power systems," *Protection and Control of Modern Power Systems*, vol. 8, no. 2, pp. 1-12, Apr. 2023.

[4] B. Yang, B. Liu, and H. Zhou *et al*., "A critical survey of technologies of large offshore wind farm integration: Summary, advances, and perspectives," *Protection and Control of Modern Power Systems*, vol. 7, no. 2, pp. 1-3, Apr. 2022.

[5] B. Zaker, G. B. Gharehpetian, and M. Karrari *et al*., "Simultaneous parameter identification of synchronous generator and excitation system using online measurements," *IEEE Transactions on Smart Grid*, vol. 7, no. 3, pp. 1230-1238, Oct. 2015.

[6] S. Veinović, D. Stojić, and L. Ivanović, "Optimized PIDD2 controller for AVR systems regarding robustness," *International Journal of Electrical Power & Energy Systems*, vol. 145, Feb. 2023.

[7] S. Mokred, Y. Wang, and T. Chen, "A novel collapse prediction index for voltage stability analysis and contingency ranking in power systems," *Protection and Control of Modern Power Systems*, vol. 8, no. 1, pp. 1-27, Jan. 2023.

[8] A. Boričić, J. L. R. Torres, and M. Popov, "Comprehensive review of short-term voltage stability evaluation methods in modern power systems," *Energies*, vol. 14, no. 14, Jul. 2021.

[9] Y. Zhou, J. An, and G. Mu *et al*., "An improved constraint-inference approach for causality exploration of power system transient stability," *Protection and Control of Modern Power Systems*, vol. 8, no. 4, pp. 1-12, Oct. 2023.

[10] V. Mukherjee and S. P. Ghoshal, "Comparison of intelligent fuzzy based AGC coordinated PID controlled and PSS controlled AVR system," *International Journal of Electrical Power & Energy Systems*, vol. 29, no. 9, pp. 679-689, Nov. 2007.

[11] P. K. Ray, S. R. Paital, and A. Mohanty *et al*., "A hybrid firefly-swarm optimized fractional order interval type-2 fuzzy PID-PSS for transient stability improvement," *IEEE Transactions on Industry Applications*, vol. 55, no. 6, pp. 6486-6498, Aug. 2019.

[12] S. Singh, S. Saini, and S. K. Gupta *et al*., "Solar-PV inverter for the overall stability of power systems with intelligent MPPT control of DC-link capacitor voltage," *Protection and Control of Modern Power Systems*, vol. 8, no. 1, pp. 1-20, Jan. 2023.

[13] G. Cai, S. Zhou, and C. Liu *et al*., "Hierarchical under frequency load shedding scheme for inter-connected power systems," *Protection and Control of Modern Power Systems*, vol. 8, no. 2, pp. 1-12, Apr. 2023.

[14] Q. Lu, S. Mei, and Y. Sun, "Nonlinear robust excitation control of large-scale generator units," in *Nonlinear Control of Power Systems*, 2nd ed., Beijing, China: Tsinghua University Press, 2008, pp. 291-306.

[15] H. Zhang, F. Shi, and Y. Liu, "Enhancing optimal excitation control by adaptive fuzzy logic rules," *International Journal of Electrical Power & Energy Systems*, vol. 63, pp. 226-235, Dec. 2014.

[16] S. K. Ghosh, T. K. Roy, and M. A. H. Pramanik *et al*., "A robust linear optimal state feedback controller design for

excitation systems of synchronous generators in single machine power systems with parametric uncertainties," in *2021 IEEE Industry Applications Society Annual Meeting (IAS)*, Vancouver, Canada, Jan. 2021, pp. 1-6.

[17] Y. Zou, W. Hu, and Z. Xiao *et al.*, "Design of intelligent nonlinear robust controller for hydro-turbine governing system based on state-dynamic-measurement hybrid feedback linearization method," *Renewable Energy*, Mar. 2023.

[18] F. Dao, Y. Zou, and Y. Zeng *et al.*, "An intelligent CPSOGSA-based mixed H2/H∞ robust controller for the multi-hydro-turbine governing system with sharing common penstock," *Renewable Energy*, Apr. 2023.

[19] H. Bevrani, "Frequency robust regulation based on multi-objective control," in *Robust power system frequency control*, 2nd ed., New York, USA: Springer, 2014, pp. 93-112.

[20] J. Machowski, Z. Lubosny, and J. W. Bialek *et al.*, "Power system components," in *Power system dynamics: stability and control*, New York, USA: John Wiley & Sons, 2020, pp. 13-56.

[21] L. Sun and B. Yang, "Design of robust sliding mode controller for power system based on disturbance observer," *Power System Protection and Control*, vol. 48, no. 20, pp. 124-132, Oct. 2020. (in Chinese)

[22] H. Lomei, D. Sutanto, and K. M. Muttaqi *et al.*, "An optimal robust excitation controller design considering the uncertainties in the exciter parameters," *IEEE Transactions on Power Systems*, vol. 32, no. 6, pp. 4171-4179, Feb. 2017.

[23] D. Stojic, T. Tarczewski, and D. Joksimovic *et al.*, "Robust synchronous generator excitation based on novel feedforward control," *International Transactions on Electrical Energy Systems*, vol. 27, no. 9, May 2017.

[24] M. Modabbernia, B. Alizadeh, and A. Sahab *et al.*, "Robust control of automatic voltage regulator (AVR) with real structured parametric uncertainties based on H_∞ and μ-analysis," *ISA transactions*, vol. 100, pp. 46-62, May 2020.

[25] S. Mei, T. Shen, and W. Hu *et al.*, "Robust H∞ control of a Hamiltonian system with uncertainty and its application to a multi-machine power system," *IEE Proceedings-Control Theory and Applications*, vol. 152, no. 2, pp. 202-210, Mar. 2005.

[26] Y. Peng, Q. M. Zhu, and H. Nouri, "Robust H2 power system stabilizer design using LMI techniques," in *Proceedings of 2011 International Conference on Modelling, Identification and Control*, Shanghai, China, Aug. 2011, pp. 405-410.

[27] H. Calgan and M. Demirtas, "A robust LQR-FOPIλDμ controller design for output voltage regulation of stand-alone self-excited induction generator," *Electric Power Systems Research*, vol. 196, Jul. 2021.

[28] M. Modabbernia, B. Alizadeh, and A. Sahab *et al.*, "A novel robust strategy for the concurrent control of frequency and voltage in the synchronous generator with real structured uncertainties," *Electric Power Components and Systems*, vol. 50, no. 16-17, pp. 1029-1050, Jun. 2022.

[29] K. Ellithy, S. Said, and O. Kahlout, "Design of power system stabilizers based on μ-controller for power system stability enhancement," in *2013 3rd International Conference on Electric Power and Energy Conversion Systems*, Istanbul, Turkey, Oct. 2013, pp. 1-6.

[30] J. M. Fard, "Robust multi-objective control of power system stabilizer using mixed H_2/H_∞ and μ analysis," *International Journal of Electrical and Computer Engineering*, vol. 8, no. 6, pp. 4800-4809, Dec. 2018.

[31] S. Furuya and J. Irisawa, "LMI-based mixed H2/H∞ controller design with regional pole constraints for damping power system oscillations," *IEEJ Transactions on Power and Energy*, vol. 124, no. 7, pp. 920-930, 2004.

[32] S. Das and I. Pan, "On the mixed H_2/H_∞ loop-shaping tradeoffs in fractional-order control of the AVR system," *IEEE Transactions on Industrial Informatics*, vol. 10, no. 4, pp. 1982-1991, May 2014.

[33] J. E. Caicedo, D. Agudelo-Martínez, and E. Rivas-Trujillo *et al.*, "A systematic review of real-time detection and classification of power quality disturbances," *Protection and Control of Modern Power Systems*, vol. 8, no. 1, pp. 1-37, Jan. 2023.

[34] V. Mortezapour, S. Golshannavaz, and E. Pouresmaeil *et al.*, "A new hybrid control technique for operation of DC microgrid under islanded operating mode," *Protection and Control of Modern Power Systems*, vol. 7, no. 4, pp. 1-11, Oct. 2022.

[35] S. Zhao, F. Blaabjerg, and H. Wang, "An overview of artificial intelligence applications for power electronics," *IEEE Transactions on Power Electronics*, vol. 36, no. 4, pp. 4633-4658, Apr. 2020.

[36] B. Youn and D. Sun, "Fuzzy PID control technology for synchronous generator excitation," *International Journal of Control and Automation*, vol. 8, no. 10, pp. 91-98, Oct. 2015.

[37] J. Ansari, A. R. Abbasi, and M. H. Heydari *et al.*, "Simultaneous design of fuzzy PSS and fuzzy STATCOM controllers for power system stability enhancement," *Alexandria Engineering Journal*, vol. 61, no. 4, pp. 2841-2850, Apr. 2022.

[38] A. J. Al Gizi, M. W. Mustafa, and K. M. Al Zaidi *et al.*, "Integrated PLC-fuzzy PID simulink implemented AVR system," *International Journal of Electrical Power & Energy Systems*, vol. 69, pp. 313-326, Jul. 2015.

[39] A. Hekimoğlu, "Sine-cosine algorithm-based optimization for automatic voltage regulator system," *Transactions of the Institute of Measurement and Control*, vol. 41, no. 6, pp. 1761-1771, Nov. 2019.

[40] S. Ekinci, D. Izci, and E. Eker *et al.*, "An effective control design approach based on novel enhanced aquila optimizer for automatic voltage regulator," *Artificial Intelligence Review*, vol. 56, no. 2, pp. 1731-1762, Jun. 2023.

[41] M. Micev, M. Ćalasan, and Z. M. Ali *et al.*, "Optimal design of automatic voltage regulation controller using hybrid simulated annealing-Manta ray foraging optimization algorithm," *Ain Shams Engineering Journal*, vol. 12, no. 1, pp. 641-657, Mar. 2021.

[42] T. A. Jumani, M. W. Mustafa, and Z. Hussain *et al.*, "Jaya optimization algorithm for transient response and stability enhancement of a fractional-order PID based automatic voltage regulator system," *Alexandria Engineering Journal*, vol. 59, no. 4, pp. 2429-2440, Aug. 2020.

[43] M. Elsisi, "Design of neural network predictive controller based on imperialist competitive algorithm for automatic voltage regulator," *Neural Computing and Applications*, vol. 31, no. 9, pp. 5017-5027, Sept. 2019.
[44] W. Aribowo, "Focused time delay neural network for tuning automatic voltage regulator," *EMITTER International Journal of Engineering Technology*, vol. 7, no. 1, pp. 34-43, Jun. 2019.
[45] Y. Zou, J. Qian, and Y. Zeng *et al*., "Eigen-structure assignment-based differential evolution algorithm for TS fuzzy control tuning applied to water-turbine governing system," *IEEE Access*, vol. 9, pp. 39322-39332, Mar. 2021.
[46] A. T. Nguyen, T. Taniguchi, and L. Eciolaza *et al*., "Fuzzy control systems: past, present and future," *IEEE Computational Intelligence Magazine*, vol. 14, no. 1, pp. 56-68, Jan. 2019.
[47] M. Khishe and M. R. Mosavi, "Classification of underwater acoustical data set using neural network trained by chimp optimization algorithm," *Applied Acoustics*, vol. 157, Jan. 2020.
[48] T. K. Roy, M. A. Mahmud, and A. M. Oo, "Robust adaptive backstepping excitation controller design for higher-order models of synchronous generators in multimachine power systems," *IEEE Transactions on Power Systems*, vol. 34, no. 1, pp. 40-51, Sept. 2018.
[49] T. K. Roy, M. A. Mahmud, and W. Shen *et al*., "Nonlinear adaptive excitation controller design for multimachine power systems with unknown stability sensitive parameters," *IEEE Transactions on Control Systems Technology*, vol. 25, no. 6, pp. 2060-2072, Mar. 2016.
[50] B. V. Patil, L. P. M. I. Sampath, and A. Krishnan *et al*., "Decentralized nonlinear model predictive control of a multimachine power system," *International Journal of Electrical Power & Energy Systems*, vol. 106, pp. 358-372, Mar. 2019.
[51] Y. Zheng, J. Zhou, and W. Zhu *et al*., "Design of a multi-mode intelligent model predictive control strategy for hydroelectric generating unit," *Neurocomputing*, vol. 207, pp. 287-299, Sept. 2016.
[52] M. A. Mahmud, M. J. Hossain, and H. R. Pota *et al*., "Robust partial feedback linearizing excitation controller design for multimachine power systems," *IEEE Transactions on Power Systems*, vol. 32, no. 1, pp. 3-16, Apr. 2016.
[53] T. K. Roy, M. A. Mahmud, and W. Shen *et al*., "Robust nonlinear adaptive backstepping excitation controller design for rejecting external disturbances in multimachine power systems," *International Journal of Electrical Power & Energy Systems*, vol. 84, pp. 76-86, Jan. 2017.
[54] R. Patel, F. Hafiz, and A. Swain *et al*., "Nonlinear excitation control of diesel generator: a command filter backstepping approach," *IEEE Transactions on Industrial Informatics*, vol. 17, no. 7, pp. 4809-4817, Aug. 2020.
[55] A. Abbadi, L. Nezli, and D. Boukhetala, "A nonlinear voltage controller based on interval type 2 fuzzy logic control system for multimachine power systems," *International Journal of Electrical Power & Energy Systems*, vol. 45, no. 1, pp. 456-467, Feb. 2013.
[56] F. Ahsan, N. H. Dana, and S. K. Sarker *et al*., "Data-driven next-generation smart grid towards sustainable energy evolution: techniques and technology review," *Protection and Control of Modern Power Systems*, vol. 8, no. 3, pp. 1-42, Jul. 2023.
[57] L. Abualigah, M. Shehab, and M. Alshinwan *et al*., "Salp swarm algorithm: a comprehensive survey," *Neural Computing and Applications*, vol. 32, pp. 11195-11215, Nov. 2020.
[58] G. I. Sayed, G. Khoriba, and M. H. Haggag, "A novel chaotic salp swarm algorithm for global optimization and feature selection," *Applied Intelligence*, vol. 48, pp. 3462-3481, Mar. 2018.
[59] M. A. Tawhid and A. M. Ibrahim, "Improved salp swarm algorithm combined with chaos," *Mathematics and Computers in Simulation*, vol. 202, pp. 113-148, Dec. 2022.
[60] A. Ateya, A. Muthanna, and A. Vybornova *et al*., "Chaotic salp swarm algorithm for SDN multi-controller networks," *Engineering Science and Technology, an International Journal*, vol. 22, no. 4, pp. 1001-1012, Aug. 2019.
[61] J. Wu, R. Nan, and L. Chen, "Improved salp swarm algorithm based on weight factor and adaptive mutation," *Journal of Experimental & Theoretical Artificial Intelligence*, vol. 31, no. 3, pp. 493-515, May 2019.
[62] M. J. Morshed, Z. Sardoueinasab, and A. Fekih, "A coordinated control for voltage and transient stability of multi-machine power grids relying on wind energy," *International Journal of Electrical Power & Energy Systems*, vol. 109, pp. 95-109, Jul. 2019.